

CMS Draft Analysis Note

The content of this note is intended for CMS internal use and distribution only

2010/05/31

Head Id: 6782

Archive Id: 7138M

Archive Date: 2010/05/25

Archive Tag: trunk

Search for Dijet Resonances in the Dijet Mass Distribution in pp Collisions at $\sqrt{s} = 7$ TeV

Robert M Harris¹, Ken Hatakeyama⁶, Bora Isildak⁴, Shabnam Jabeen⁸, Chiyoun Jeong³,
Konstantinos Kousouris¹, Sung-Won Lee³, Kalanand Mishra¹, Sertac Ozturk², Kai Yi⁵, and
Marek Zielinski⁷

¹ Fermilab, Batavia, IL, USA

² University of Cukurova, Adana, Turkey

³ Texas Tech University, Lubbock, TX, USA

⁴ Bogazici University, Istanbul, Turkey

⁵ University of Iowa, Iowa City, IA, USA

⁶ Baylor University, Baylor, TX, USA

⁷ University of Rochester, Rochester, NY, USA

⁸ Brown University, Providence, RI, USA

Abstract

We present a measurement of the dijet invariant mass spectrum and search for new particles decaying to dijets at CMS in pp collisions at $\sqrt{s} = 7$ TeV with 7.2 nb^{-1} of data collected in the April - May 2010 running period. The dijet mass distribution of the two leading jets in the pseudorapidity region $|\eta| < 1.3$ is measured and compared to QCD predictions from PYTHIA and the CMS detector simulation. We fit the observed dijet mass spectrum with a parameterization, search for dijet resonances, and set upper limits at 95% CL on the resonance cross section. These generic cross section limits are compared with theoretical predictions for the cross section for several models of new particles: axigluons, flavor universal colorons, excited quarks, E6 diquarks, Randall Sundrum Gravitons, W' and Z' .

This box is only visible in draft mode. Please make sure the values below make sense.

PDFAuthor: Dijet Group
PDFTitle: Search for Dijet Resonances in the Dijet Mass Distribution in pp Collisions
at $s=7$ TeV
PDFSubject: CMS
PDFKeywords: CMS, physics, software, computing

Please also verify that the abstract does not use any user defined symbols

DRAFT

Contents

1	1	Introduction	2
2	1.1	Motivation	2
3	1.2	Models	2
4	1.3	Summary of Experimental Technique	3
5	2	Measurement of Dijet Mass Spectrum	4
6	2.1	Data Sample	4
7	2.2	MC Sample	5
8	2.3	Jet Reconstruction	5
9	2.4	Event Selection	5
10	2.5	Dijet Mass Spectrum	6
11	2.6	Dijet Mass Spectrum and Fit	12
12	3	Search for Dijet Resonance	17
13	3.1	The Signal: Dijet Resonance	17
14	3.2	Largest Fluctuation and Significance	21
15	3.3	Setting Cross Section Upper Limits	24
16	4	Systematic Uncertainties	26
17	4.1	Jet Energy Scale (JES)	26
18	4.2	Jet Energy Resolution (JER)	27
19	4.3	Background Parameterization	29
20	4.4	Total Uncertainty	29
21	4.5	Incorporating Systematics in the Limit	29
22	5	Results	31
23	6	Expected Future Limits	33
24	7	Expected Future Limits	36
25	8	Conclusions	39
26	A	Resonance Model Cross Sections	40
27	B	Binning and Data Table	41
28	C	Event Displays of High Mass Dijet Events	42
29	D	Likelihood Distributions	46
30			

1 Introduction

In this note we document our first measurement of the dijet mass distribution and our first search for dijet resonances in pp Collisions at $\sqrt{s} = 7$ TeV. The note is also intended as documentation for a Physics Analysis Summary document for approved CMS results for the ICHEP conference in July 2010. This draft is based on 7.2 nb^{-1} of data, but is expected to be updated periodically as the data accumulates towards ICHEP. Please also see previous documents on simulation of the complete analysis at $\sqrt{s} = 10$ TeV [1, 2] and at $\sqrt{s} = 14$ TeV [3]. This analysis is synchronized with a simultaneous analysis of the dijet centrality ratio [4], which provides a simple measure of the angular distribution in the same mass bins, in order to confirm and understand the new physics which is expected to emerge simultaneously in both analyses [5].

1.1 Motivation

Our experimental motivation is to make a first measurement of the dijet mass distribution and see whether it agrees with expectations or contains new physics beyond the Standard Model (SM). The LHC is a parton-parton collider in a previously unexplored energy region. If new parton-parton resonances exist at sufficiently low mass then the LHC will produce them copiously. These resonances must also decay to partons giving two jets in the final state. One theoretical motivation is that the SM has important unanswered questions. Why do quarks come in different flavors? Why are the quarks arranged in generations? Why are there four different forces? How do we unify gravitation with the other forces? Why is gravity so weak? Models that try to address these questions often predict short-lived particles that can decay to two partons: dijet resonances.

1.2 Models

We search for processes producing narrow resonances, X , decaying to dijets as illustrated in fig. 1: $pp \rightarrow X \rightarrow \text{jet} + \text{jet}$ (inclusive).

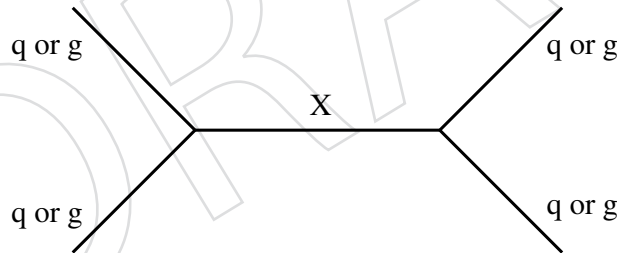


Figure 1: Feynman Diagram of dijet resonance. The initial state and final state both contain two partons (quarks, antiquarks or gluons) and the intermediate state contains an s -channel resonance X .

We perform a generic search that we can apply to any model. Here we introduce some models in order of decreasing cross section at low mass, say a few words about the cross section, and explicitly list the partons involved in production and decay, as previously written [3]. Excited states of composite quarks [6] are strongly produced giving large cross sections ($qg \rightarrow q^*$). Axigluons [7] or colorons [8] from an additional color interaction are also strongly produced, but require an antiquark in the initial state ($q\bar{q} \rightarrow A$ or C) slightly reducing the cross section compared to excited quarks. Diquarks [9] from superstring inspired E_6 grand unified models are produced with electromagnetic coupling from the valence quarks of the proton ($ud \rightarrow D$). The cross section for E_6 diquarks at high mass is the largest of all the models considered, because at high parton momentum the probability of finding a quark in the proton is significantly larger

than the probability of finding a gluon or antiquark. Randall Sundrum gravitons [10] from a model of large extra dimensions are produced from gluons or quark-antiquark pairs in the initial state ($q\bar{q}, gg \rightarrow G$). Heavy W bosons [11] inspired by left-right symmetric grand unified models have electroweak couplings and require antiquarks for their production ($q_1\bar{q}_2 \rightarrow W'$), giving small cross sections. Heavy Z bosons [11] inspired by grand-unified models are widely anticipated by theorists, but they are electroweakly produced, and require an antiquark in the initial state ($q\bar{q} \rightarrow Z'$), so their production cross section is around the lowest of the models considered. Table 1 summarizes some properties of these models.

Model Name	X	Color	J^P	$\Gamma/(2M)$	Chan
Excited Quark	q^*	Triplet	$1/2^+$	0.02	qg
E_6 Diquark	D	Triplet	0^+	0.004	qq
Axigluon	A	Octet	1^+	0.05	$q\bar{q}$
Coloron	C	Octet	1^-	0.05	$q\bar{q}$
RS Graviton	G	Singlet	2^-	0.01	$q\bar{q}, gg$
Heavy W	W'	Singlet	1^-	0.01	$q\bar{q}$
Heavy Z	Z'	Singlet	1^-	0.01	$q\bar{q}$

Table 1: Properties of Some Resonance Models

Published lower limits [12] on the mass of these models in the dijet channel are listed in table 2.

q^*	A or C	D	ρ_{T8}	W'	Z'	G
0.87	1.25	0.63	1.1	0.84	0.74	-

Table 2: Published lower limits in TeV on the mass of new particles considered in this analysis. These 95% confidence level exclusions from the Tevatron [12] are the best published limits in the dijet channel.

1.3 Summary of Experimental Technique

Our experimental technique starts with a measurement of the inclusive process $pp \rightarrow \text{jet} + \text{jet} + \text{anything}$. Inclusive means we measure processes containing at least two jets in the final state, but the events are allowed to contain additional jets, or anything else. The dijet in the event is simply the two highest p_T jets, the leading jets. Within the standard model our dataset is expected to be overwhelming dominated by the $2 \rightarrow 2$ process of hard parton scatters, with additional radiation off the initial and final state partons naturally giving additional jets. We do not cut away events that contain this radiation, which would reduce signals that also have similar amounts of radiation, and un-necessarily restrict signals to a narrow topology. The events can also contain additional particles, such as leptons or photons, but this will occur very rarely in the standard model. Finally, even more rarely within the standard model, the two leading CaloJets in the event can result from electrons, photons or taus producing energy in the calorimeter, and we do not exclude these insignificant contributions to our sample either. Our dijet selection is then open to many signals of new physics including high p_T jets, leptons and photons. However, our selection is optimized for signals in the $2 \rightarrow 2$ parton scattering process, and is overwhelmingly dominated by the signal background of dijets from QCD within the standard model.

Our experimental method to search for dijet resonances utilizes the dijet mass spectrum measured from the two leading jets in the data. If a dijet resonance exists, it should appear in

the dijet mass spectrum as a bump. First we compare the dijet mass spectrum to QCD predictions from PYTHIA to see if they agree, but we do not use QCD to model our background in the search. We use a smooth parameterization to model our background. We fit the dijet mass spectrum with a smooth parameterization and see whether we can get a good fit. The fit probability tells us whether the data is smooth, which is the first test for the presence of a resonance. We look at the difference between the data and the fit, and estimate the significance of the largest upward fluctuation in the data interpreted as a narrow resonance. If there is no significant evidence for dijet resonances, we proceed to set limits. The dijet resonance shape for generic di-parton resonances containing qq, qg and gg partons were simulated using PYTHIA as resonance signals. To calculate the upper cross section limit for this dijet resonance shape in our data, we use a binned maximum likelihood method. The method gives a Poisson likelihood as a function of the cross section. We convolute the statistical likelihood distribution with our Gaussian systematic uncertainty and find the 95% confidence level upper limit on the cross section. This gives cross section limits for generic narrow qq, qg and gg resonances, independent of any specific resonance model. The upper limit on the cross section is then compared with the predicted cross section for a few benchmark models to obtain mass limits on particular models. This experimental method is basically the same as that employed by the dijet resonances searches at the Tevatron [12–14].

2 Measurement of Dijet Mass Spectrum

In this section we explain how we measure the dijet mass spectrum in data, compare it with the Monte Carlo predictions for QCD, and fit it to a simple parameterization to test the smoothness of the data.

2.1 Data Sample

Our collision dataset was

/MinimumBias/Commissioning10-SD_JetMETTau-v9/RECO

we run over this dataset at the Fermilab LPC and select the following good runs taken during April-May 2010:

133874–133877, 133881, 133885, 133927, 133928, 135149, 135175,
135445, 135521, 135523, 135525, 135528, 135534, 135535, 135537

The good run selection is based on the CMS Run Registry database. In particular, we require that runs have offline data quality monitoring flags set as GOOD for the following components: L1,HLT,ECAL,HCAL,TRACKER,PIXEL,JETMET. The integrated luminosity of the selected sample is estimated to be 7.2 nb^{-1} .

We make the following Technical Trigger bit selections for this sample: 0 AND NOT (36 OR 37 OR 38 OR 39) which select events consistent with the LHC bunch crossing and veto events from Beam Halo. We apply scraping event removal and a preselection that requires each event to have at least one jet with raw $p_T > 4 \text{ GeV}$. This preselection job writes out root trees from the InclusiveJetTreeProducer on cmslpc.fnal.gov.

2.2 MC Sample

For the comparison between data and simulation, we use the QCD Pythia MC where the phase space is divided into 20 exclusive bins, based on the transverse momentum of the hard scattered parton (\hat{p}_T). The MC samples used are:

/QCDDiJet_PtXXtoYY/Summer09-MC_31X_V9_7TeV-v1/GEN-SIM-RECO

where XX and YY stand for the \hat{p}_T boundaries. For the final comparison with the data, the MC samples are weighted according to the cross-section and the number of events that were used.

The analysis was done using the CMSSW_3.6.1 release and the software is available in the CMS cvs system, through the following tags:

V00-06-00 JetMETAnalysis/JetUtilities
V00-07-03 QCDAnalysis/HighPtJetAnalysis

2.3 Jet Reconstruction

Jets are reconstructed using the Anti-KT algorithm with cone size $R = \sqrt{(\Delta\eta)^2 + (\Delta\phi)^2} = 0.7$. Below we will discuss three types of jets: reconstructed, corrected and generated. The reconstructed jet energy, E , is defined as the scalar sum of the calorimeter tower energies inside the jet. The jet momentum, \vec{p} , is the corresponding vector sum: $\vec{p} = \sum E_i \hat{u}_i$ with \hat{u}_i being the unit vector pointing from the origin to the energy deposition E_i inside the cone. The jet transverse momentum, p_T , is the component of \vec{p} in the transverse plane. The E and \vec{p} of a reconstructed jet are then corrected for the non-linear response of the calorimeter to a generated jet. Generated jets come from applying the same jet algorithm to the Lorentz vectors of stable generated particles before detector simulation. The corrections are chosen so that, on average, the p_T of a corrected jet is equal to the p_T of the corresponding generated jet.

The corrections used for this analysis are the CMS standard relative (L2) and absolute(L3) jet corrections for η and p_T variation of the jet response using tag "Spring10" for the data and the tag "Summer09_ReReco332_7TeV" for the MC.

The dijet system is composed of the two jets with the highest p_T in an event (leading jets), and the dijet mass is given by $m = \sqrt{(E_1 + E_2)^2 - (\vec{p}_1 + \vec{p}_2)^2}$.

2.4 Event Selection

We run on the InclusiveJetRoot trees and produce a single processed root tree. In this step we select the Anti-KT 0.7 jets and apply the jet corrections. We select events that have passed the HLT_Jet15U trigger path and perform a dijet mass preselection of $m > 100$ GeV corrected. From the processed trees we perform the final analysis. We require there to be a good primary vertex with z value within 15 cms of the center of the detector and a number of degrees of freedom of at least 4.

Finally, we require both the leading jets to satisfy $|\eta| < 1.3$. This cut serves several purposes.

- It suppresses QCD processes significantly more than dijet resonances.
- It defines a fiducial region for our measurement predominantly in the Barrel.
- It provide a faster trigger turn on curve for the jet trigger which uses E_T , allowing us to start the analysis at lower mass.

Trigger Path	L1 seeds	Description
L1_SingleJet6U	none	1 Jet with $E_T > 6$ GeV
HLT_L1Jet6U	L1_SingleJet6U	No selections beyond L1
HLT_Jet15U	L1_SingleJet6U	A single jet trigger, requiring ≥ 1 jet at HLT with $p_T > 15$ GeV. The jet energy threshold is chosen based on uncorrected jets.

Table 3: L1 and High Level Jet Trigger Descriptions

In addition, we require that both leading jets satisfy the LOOSE jet ID which is defined below:

- jet electromagnetic fraction (EMF) > 0.01 if jet $|\eta| < 2.4$,
- number of rechits carrying 90% of the jet energy (n90hits) > 1
- fraction of energy contributed by the hottest HPD (fHPD) < 0.98

These cuts are used to make a histogram of dijet mass and other quantities (MassResults_ak7calo_SD_Jet15U.root) which is saved, along with the processed root tree (ProcessedTree_ak7calo_Jet15U.root) on cms-lpc.fnal.gov at

/uscms_data/d2/kkousour/7TeV/DijetMassAnalysis/May20th/

For the MC events, no trigger requirements are applied but the rest of the event and jet selection criteria are identical.

2.5 Dijet Mass Spectrum

2.5.1 Trigger

The trigger efficiency for the HLT path HLT_Jet15U, measured from a sample acquired with a prescaled trigger with a lower p_T threshold (HLT_L1Jet6U), was greater than 99% for dijet mass above 137 GeV as shown in Fig. 2. However, we start the Dijet Mass Spectra from 156 GeV in order to align it to the Dijet Centrality Ratio analysis [4]. In that analysis the outer eta interval does not become fully efficient for the trigger until 156 GeV.

The number of events vs. dijet mass are shown in figure 3. The trigger turn over of the HLT_Jet15U trigger can be seen in the mass spectrum along with the 156 GeV cut. The processed dijet cut of 100 GeV has been relaxed to make this plots.

2.5.2 Dijet Data Quality

The number of events in the analysis after the basic cuts are shown for each cut in table 4

Events after vertex cut	437907
Events after dijet cuts $m > 156$ GeV and $ \eta < 1.3$	4790
Events after jet id cut	4788

Table 4: Cuts and Events

The number of events rejected by Jet ID is very small, because the requirement that the two leading jets have a dijet mass $m > 156$ and $|\eta| < 1.3$ GeV enhances the jet purity. After all cuts, we present some basic distributions indicating jet and event quality in Fig. 4. The basic distributions look fine. The dijet events have low $MET/\Sigma E_T$ indicating that the event energy is well balanced in the transverse plane. EMF, the fraction of jet energy in the ECAL, is distributed smoothly for the two leading jets, with no peaks near either zero or one which would indicate a problem from the HCAL or ECAL. The two leading jets are back-to-back in ϕ as expected for

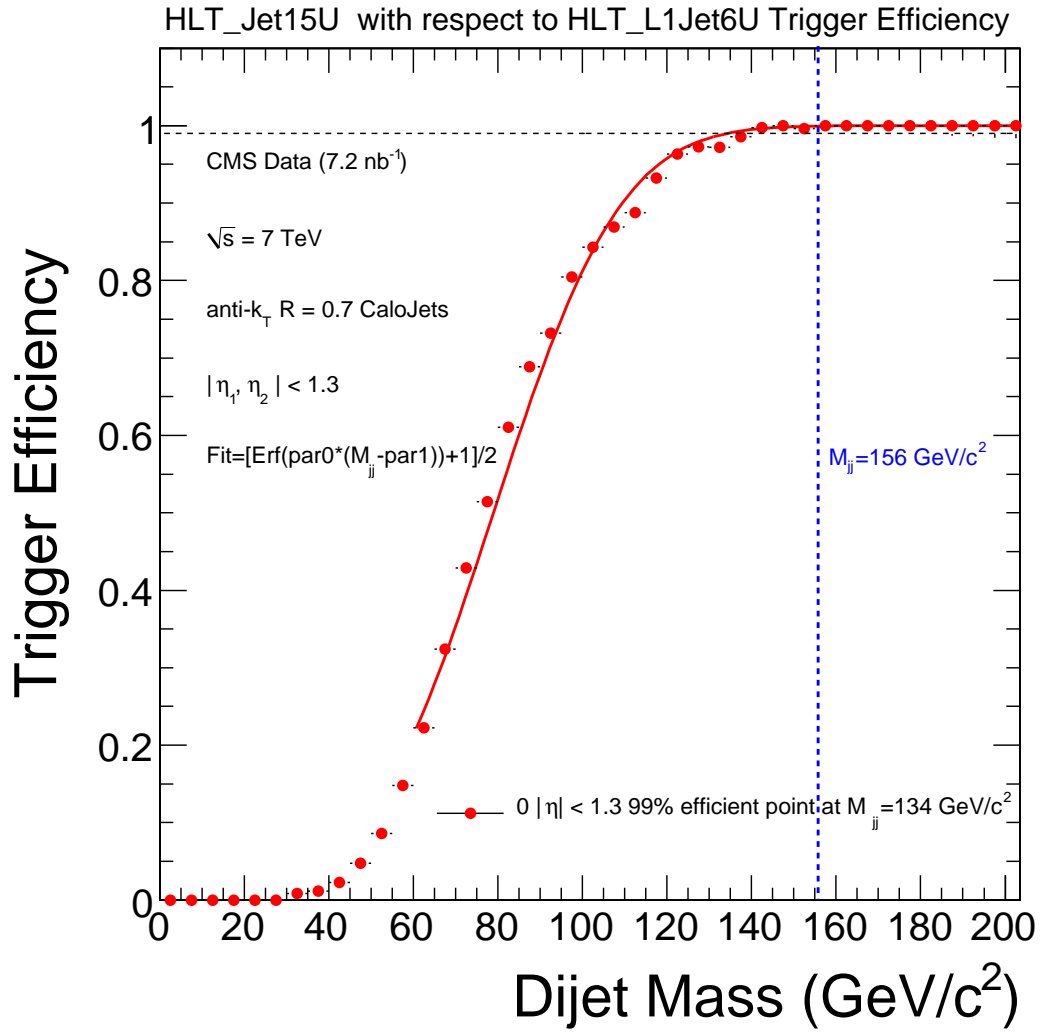


Figure 2: HLT_Jet15U trigger efficiency as a function of dijet mass, shown for two intervals of pseudorapidity, one corresponding to this analysis ($|\eta| < 1.3$) and one that is important for the dijet centrality ratio $0.7 < |\eta| < 1.3$.

200 dijets. The $\eta - \phi$ distribution of two leading jets is uniform and does not show any indication of
 201 hot or dead regions of the calorimeter. The η distribution of the two leading jets is smooth and
 202 demonstrates the characteristic forward peaks from Rutherford-like QCD scattering at fixed
 203 invariant mass. The ϕ distribution of the two leading jets is flat.

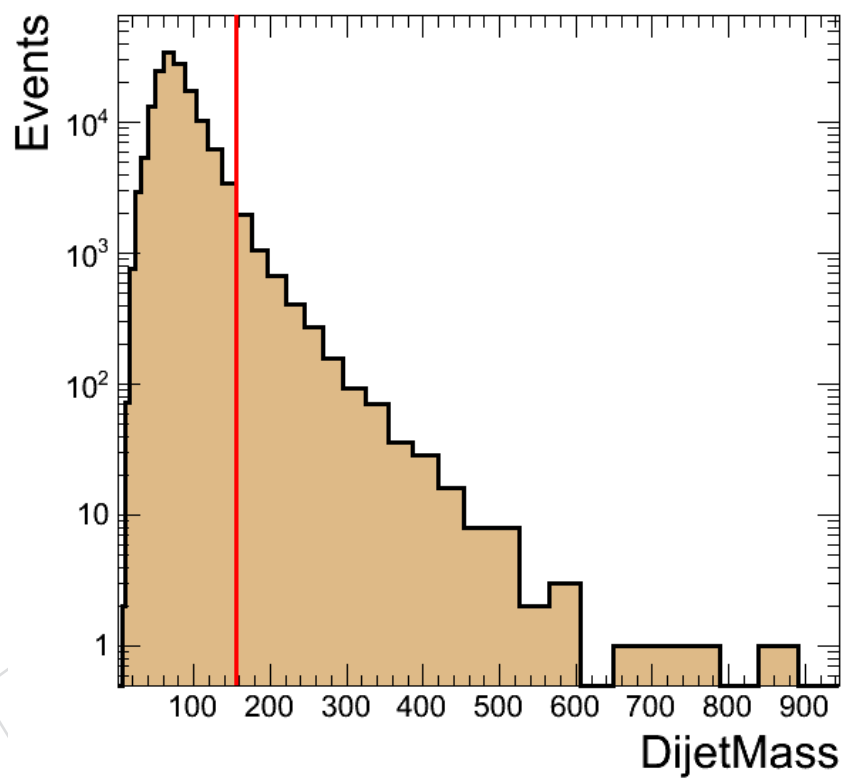


Figure 3: Number of events vs. dijet mass (histogram) requiring all cuts except the final dijet mass cut for trigger efficiency at $m = 156\text{GeV}$ (vertical line)

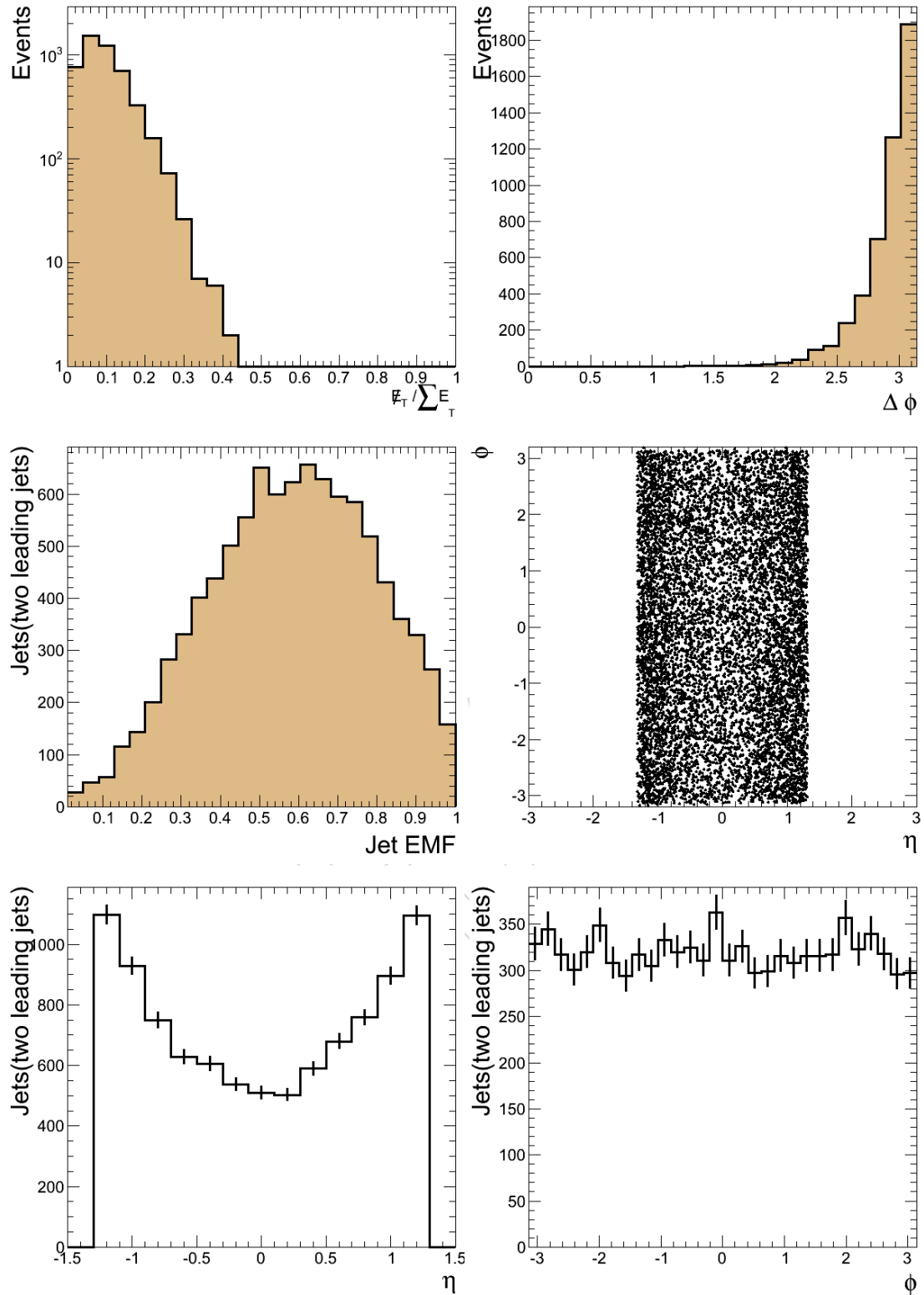


Figure 4: Basic Event and Jet Quality Distributions. upper left) Missing calorimeter E_T divided by total calorimeter E_T . upper right) The phi difference of the two leading jets. middle left) The EM energy fraction of the two leading jets. middle right) Jet ϕ vs. η for the two leading jets. lower left) The η distribution for the two leading jets. lower right) The ϕ distribution for the two leading jets

As an indication of the stability of our data as a function of run, in Fig. 5 we show the mean dijet mass after all cuts is stable. We also show the number of dijet events vs. run. Run 133927 from $5\mu b^{-1}$ of integrated luminosity has only 2 dijet events, both near the mass threshold of 156 GeV, so the mean dijet mass and its error is not well determined for run 133927.

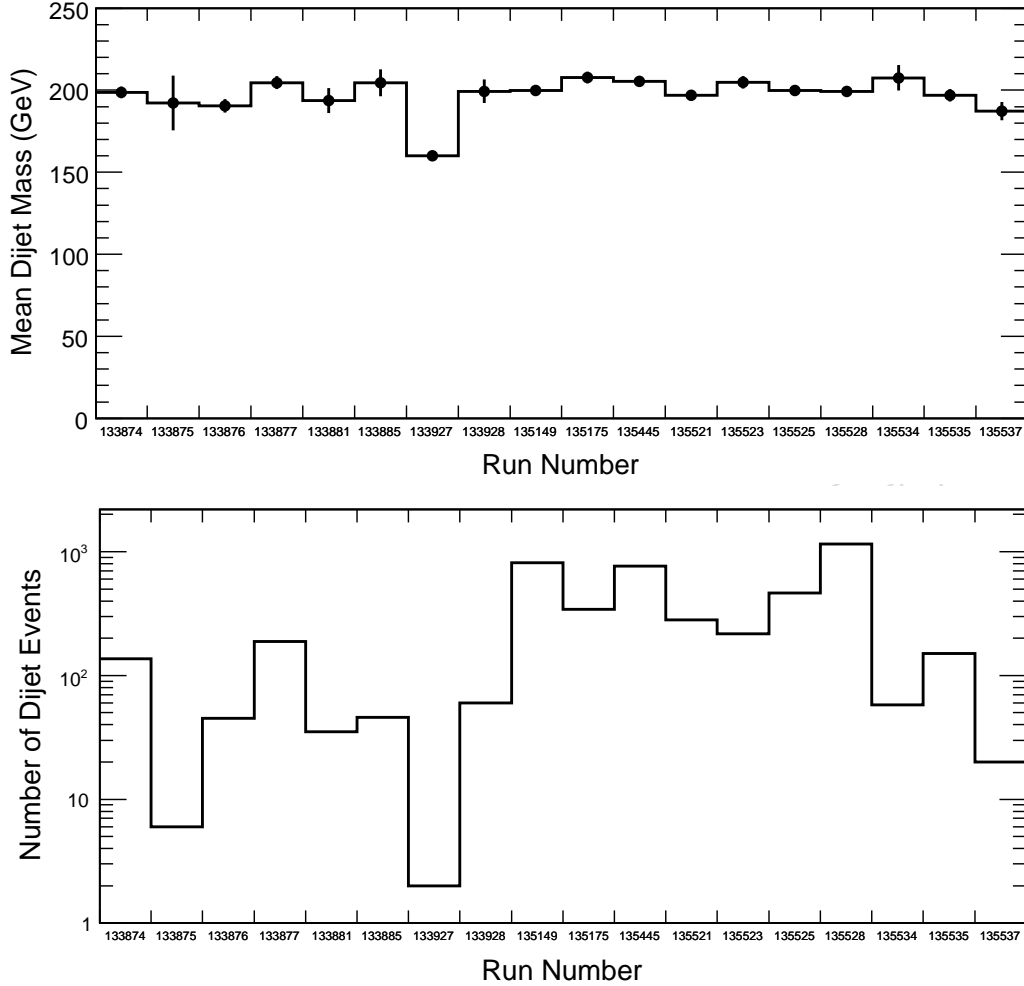


Figure 5: Mean dijet mass vs run (top) and number of events vs. run (bottom).

2.5.3 Spectrum and QCD

The measured dijet mass spectrum is shown in Fig 6. The mass spectrum is defined by

$$\frac{d\sigma}{dm} = \frac{1}{\int L dt} \frac{N_i}{\Delta m_i} \quad (1)$$

where m is the dijet mass, N_i is the number of events in the i -th dijet mass bin, and Δm_i is the width of the i -th dijet mass bin, and the integrated luminosity is $\int L dt$. This data is also tabulated in Appendix B. The bin width is approximately the dijet mass resolution, and gradually increases as a function of mass. The data is compared to a PYTHIA QCD MC prediction that has been normalized to have the same number of events as the data in this plot. This normalization of the MC is the same as multiplying the absolute normalization prediction for this

luminosity by a factor of 0.82. The shape of the PYTHIA QCD MC prediction is close to the data and there is no evidence for new physics.

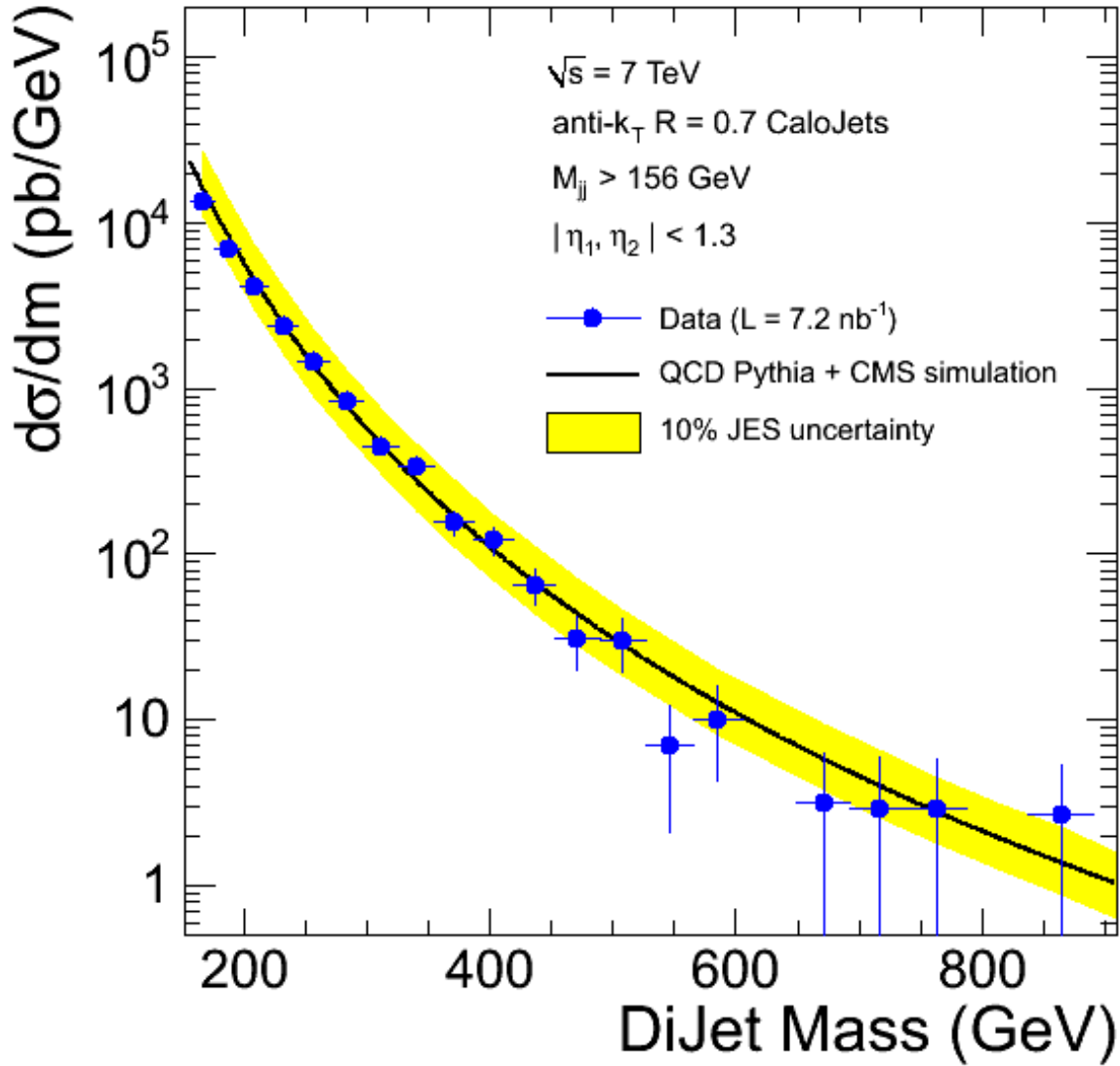


Figure 6: The dijet mass spectrum data (points) is compared to a QCD MC prediction (histogram). Both the data and QCD prediction are absolutely normalized assuming 7.2 nb $^{-1}$ of integrated luminosity. The yellow band shows the sensitivity to a 10% systematic uncertainty on the jet energy scale.

Event displays of the ten highest mass dijet events are shown in Appendix C. They all look like good dijet events, with collimated calorimeter energy deposits and associated tracks. The highest dijet mass observed is 851 GeV.

2.6 Dijet Mass Spectrum and Fit

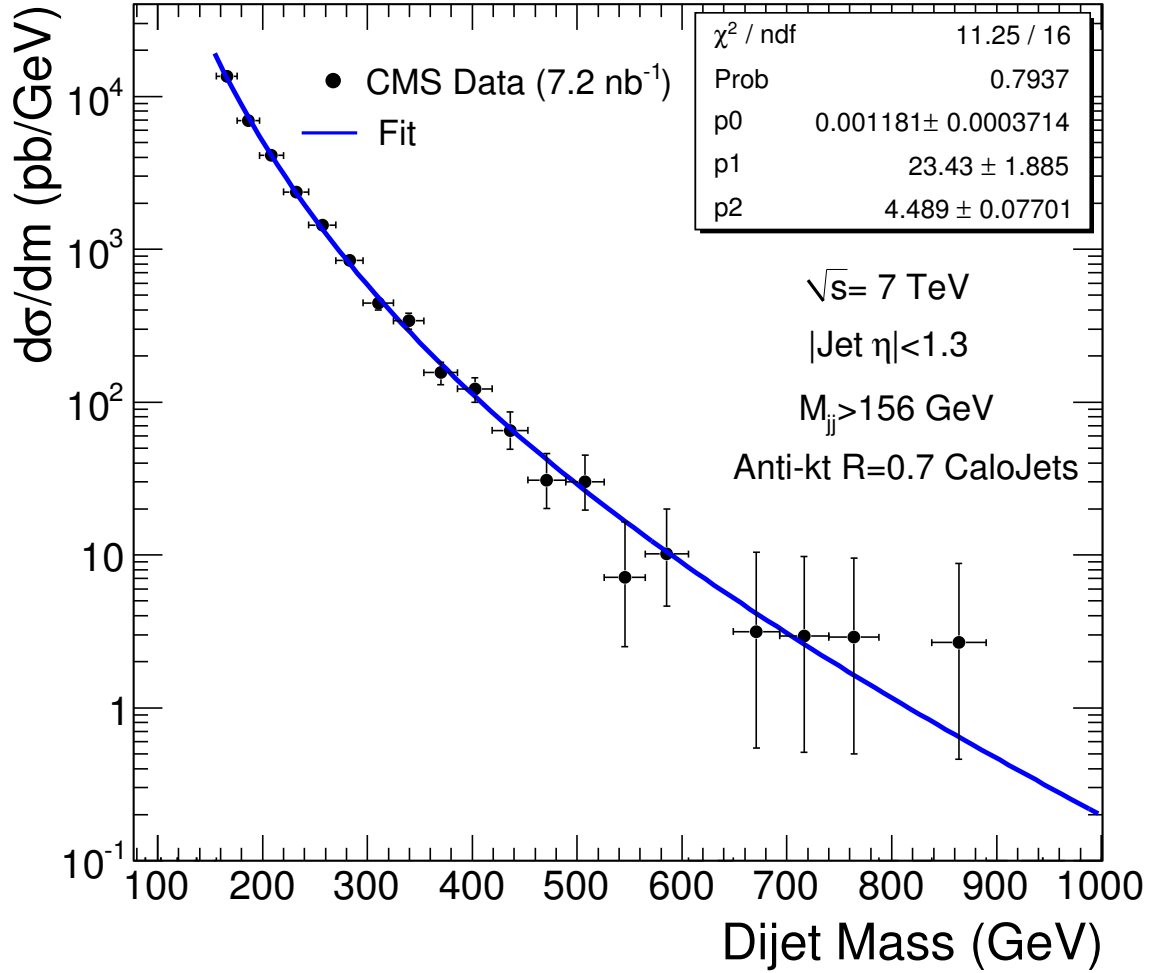


Figure 7: The dijet mass distribution (points) compared to a smooth background fit (solid curve).

Fig. 7 shows the dijet mass spectrum from Fig. 6 compared to a fit. Here we model the background to a dijet resonance coming from standard model dijet production using a simple parameterization. Our first test for whether there is a bump or other local effect in the data is to simply see if we can get a good fit to a smooth parameterization. Fig. 7 also shows the parameterization fitted to the data. We get a χ^2 of 11 for 16 degrees of freedom for the fit. The parameterization chosen is

$$\frac{d\sigma}{dm} = \frac{P_0 \cdot (1 - m/\sqrt{s})^{P_1}}{m^{P_2}} \quad (2)$$

Fig 8 shows the fractional differences between data and the fit function, $(\text{data}-\text{fit})/\text{fit}$, which show no indication of any peaks above the background fit. In the fractional difference plot the error bars are in units of the fit in the bin. Fig. 8 show the pulls, defined as $(\text{Data}-\text{Fit})/\text{Error}$, which are consistent with statistical fluctuations and are oscillating around zero. In the pulls

232 plot the error bars are always exactly 1, because they are in units of the error in the bin.

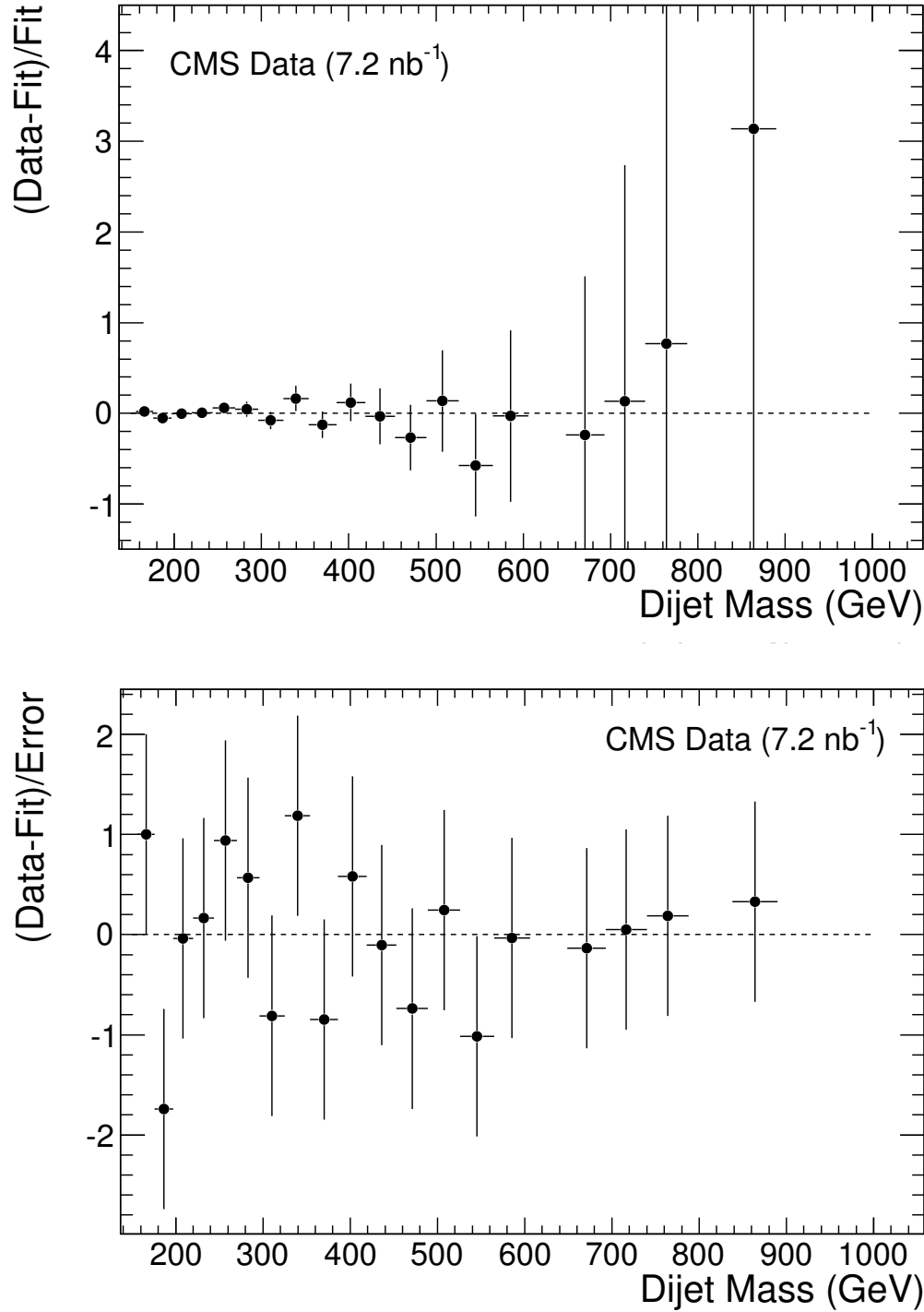


Figure 8: *Top*) The fractional difference between the dijet mass distribution (points) and a smooth background fit as a function of dijet mass. *Bottom*) The pulls distribution (Data-Fit)/Error as a function of dijet mass.

2.6.1 Fit to Dijet Mass Spectrum with Various Parametrizations

In this section we describe fit to the dijet mass distribution, $d\sigma/dm$, observed in data using various parametrizations to QCD spectrum. We start with a simple power law with two free parameters as described earlier. We then try including a term with some power of $(1 - m/\sqrt{s})$ (where $\sqrt{s} = 7$ TeV is the center-of-mass energy) to account for parton distribution functions. Finally, we also try including a term quadratic in m/\sqrt{s} to give the fit a little more flexibility to describe data at high mass tails.

These parametrizations are listed in equation 3.

$$\begin{aligned}
 \frac{d\sigma}{dm} &= \frac{P_0}{m^{P_1}}, \quad (2 - \text{parameter fit}) \\
 &= \frac{P_0 \cdot (1 - m/\sqrt{s})^{P_1}}{m^{P_2}}, \quad (3 - \text{parameter fit}) \\
 &= \frac{P_0 \cdot \left(1 - m/\sqrt{s} + P_3 \cdot (m/\sqrt{s})^2\right)^{P_1}}{m^{P_2}}. \quad (4 - \text{parameter fit}) \\
 (3)
 \end{aligned}$$

The $d\sigma/dm$ distribution in data along with fitted curve and fit results for 2-, 3-, and 4-parameter QCD dijet mass parametrization is shown in Fig. 9 (using maximum likelihood fit) and in Fig. 10 (using χ^2 minimization fit). Clearly, 2-parameter fit is insufficient to describe data at high dijet mass values. Both 3- and 4-parameter fits describe the data well. The 4-parameter fit gives almost identical result to the 3-parameter fit though it has slightly larger uncertainty band, as expected. The difference between 3-parameter fit and 4-parameter fit is much smaller than between 2-parameter fit and 3-parameter fit.

Currently we plan to use 3-parameter fit as our default because we need minimum 3 parameters to describe the QCD spectrum with the given amount of data. The uncertainty band for the fit function can be taken as a measure of the systematic uncertainty in describing the QCD background parametrization. Figures 9–10 also show the fractional differences between data and the fit function, $(\text{data-fit})/\text{fit}$, for each fit.

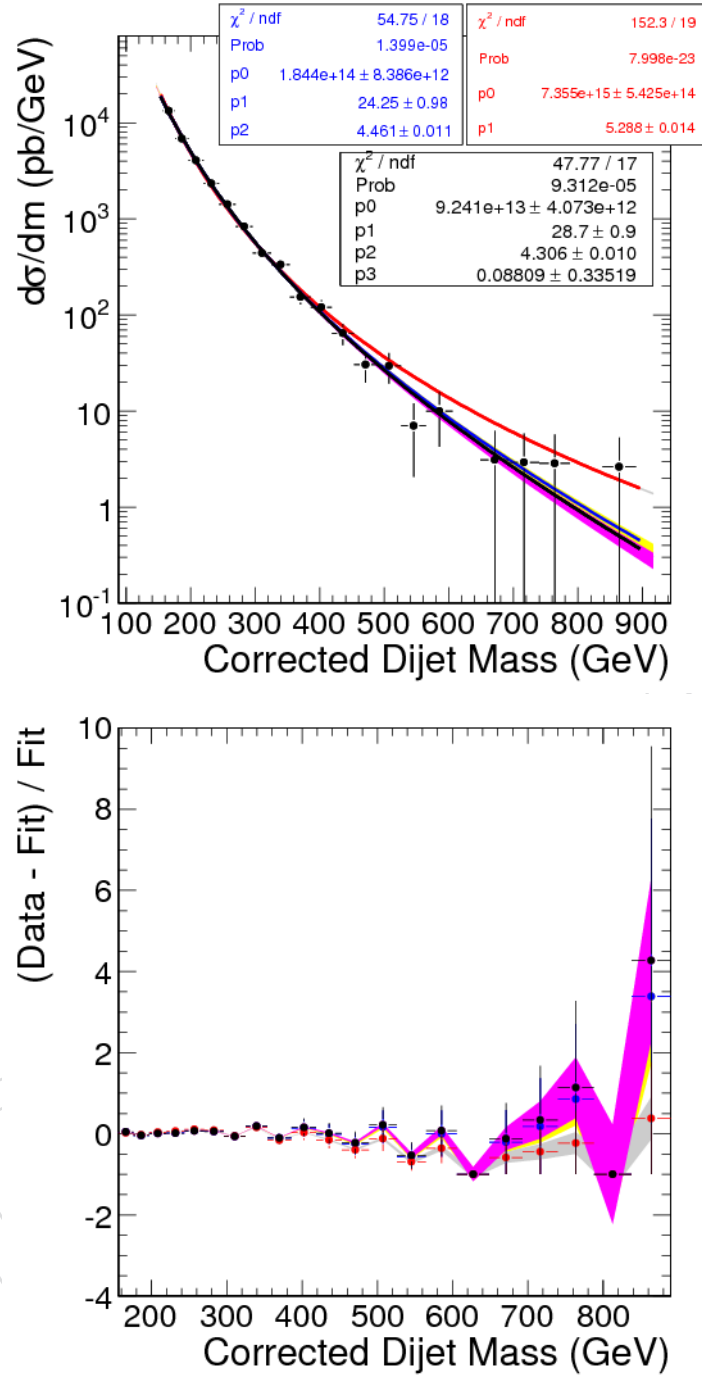


Figure 9: *Top*) Maximum likelihood fit to the dijet mass distribution, $d\sigma/dm$, observed in data (shown as solid points) using various parametrizations of QCD spectrum described by Eq. 3. The red colored curve with gray uncertainty band is from 2-parameter fit. The blue colored curve with yellow uncertainty band is from 3-parameter fit. We take this fit as our default. The black colored curve with magenta uncertainty band is from 4-parameter fit. The uncertainty band in each case was obtained by propagating the 1σ uncertainty in each fit parameter and the correlation matrix among the parameters to compute the uncertainty in the fit function. *Bottom*) Fractional difference between the dijet mass distribution data points and fit as a function of dijet mass. The red colored points correspond to 2-parameter fit, blue points correspond to 3-parameter fit, and the black points correspond to 4-parameter fit. The uncertainty band from fit is also shown in each case.

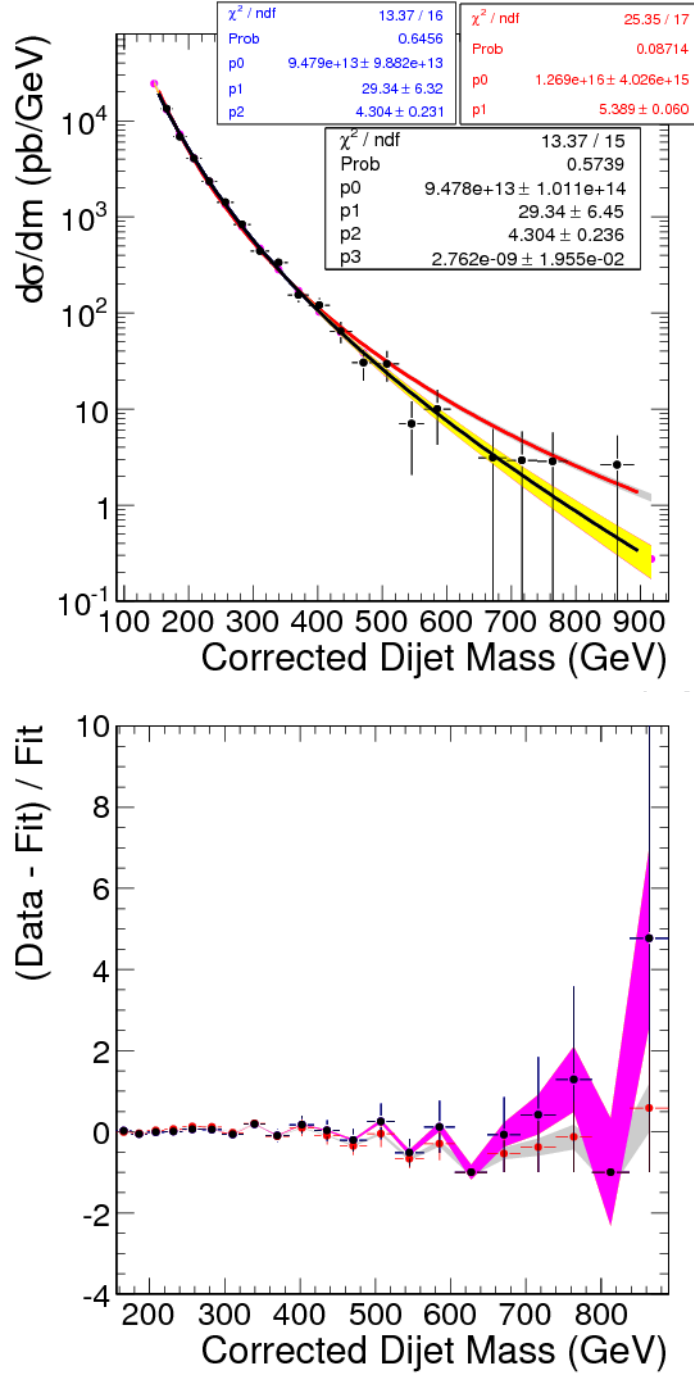


Figure 10: *Top*) χ^2 minimization fit to the dijet mass distribution, $d\sigma/dm$, observed in data (shown as solid points) using various parametrizations of QCD spectrum described by Eq. 3. The red colored curve with gray uncertainty band is from 2-parameter fit. The blue colored curve with yellow uncertainty band is from 3-parameter fit. We take this fit as our default. The black colored curve with magenta uncertainty band is from 4-parameter fit. The uncertainty band in each case was obtained by propagating the 1σ uncertainty in each fit parameter and the correlation matrix among the parameters to compute the uncertainty in the fit function. *Bottom*) Fractional difference between the dijet mass distribution data points and fit as a function of dijet mass. The red colored points correspond to 2-parameter fit, blue points correspond to 3-parameter fit, and the black points correspond to 4-parameter fit. The uncertainty band from fit is also shown in each case.

3 Search for Dijet Resonance

3.1 The Signal: Dijet Resonance

We search for narrow dijet resonances in general, rather than a specific model of dijet resonance production.

We require only a model of the resonance line shape. We will only consider narrow resonances in this analysis, for which the natural resonance width is negligible compared to the CMS dijet mass resolution, so that the natural width does not affect the resonance shape. The type of parton pairs in the resonance decay (qq , qg , or gg) does affect the resonance shape. To obtain generic shapes for these three types of parton pairings, the process of $qg \rightarrow q^* \rightarrow qg$, $q\bar{q} \rightarrow G \rightarrow q\bar{q}$ and $gg \rightarrow G \rightarrow gg$ were produced using PYTHIA+CMS simulation at three different masses of 0.7 TeV, 1.2 TeV and 2 TeV. In Fig. 11, we present these resonance shapes and also one at 0.5 TeV from extrapolation [1].

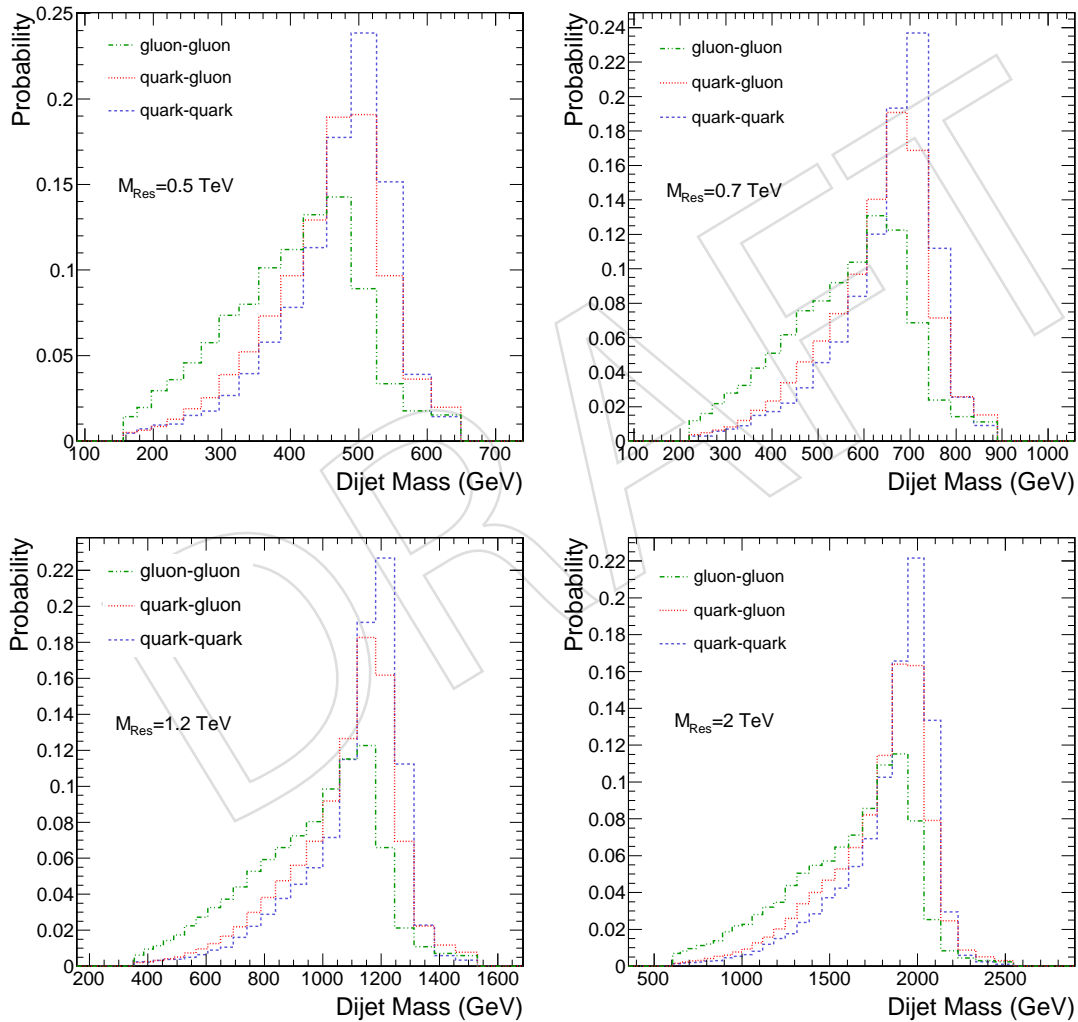


Figure 11: Dijet mass distribution for $q\bar{q}$ (qq), qg and gg resonances of mass at 1.2 TeV.

The source of the shape differences among qq , qg and gg resonances has been studied previously [2]. The width of dijet resonances increases with the number of gluons in the final state, primarily because gluons emit more radiation than quarks. The peak value of dijet mass of the

resonance decreases with the number of final state gluons, primarily due to smaller response of the CMS detector to gluon jets than to quark jets. The low mass tail of the resonance shape comes primarily from final state radiation. A small high mass tail comes from initial state radiation. These resonance shapes are approximately valid for any model of resonance involving these pairs of partons, assuming the models natural half-width ($\Gamma/2$) is small compared to the dijet mass resolution. In Fig 12 we present an estimate of the resolution of the Gaussian core of the dijet mass response distribution from fits to the peak in an interval between -0.5σ and 1.5σ .

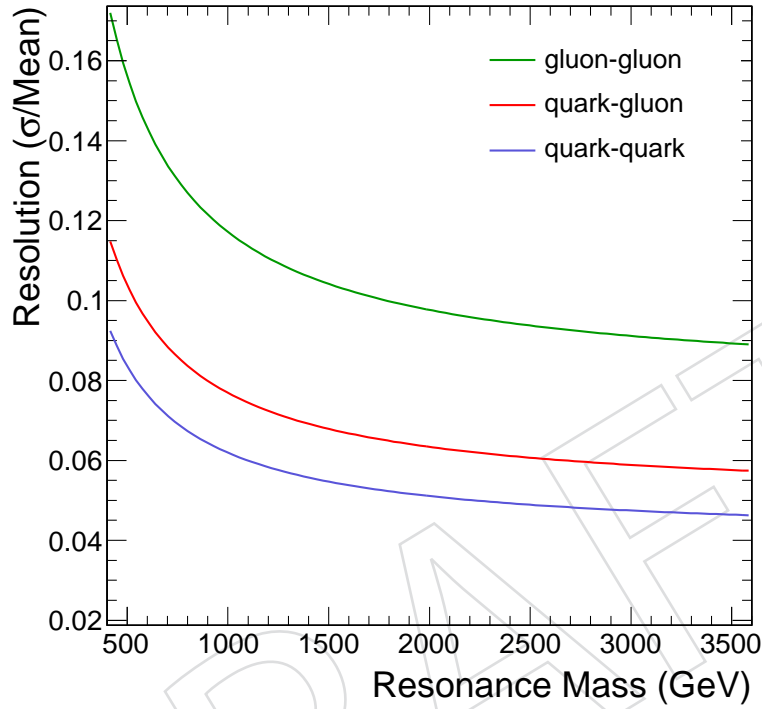


Figure 12: The fractional width of the Gaussian core of the response distribution as a function of resonance mass from CMS detector simulations of $q\bar{q}$ (qq), qg and gg dijet resonances.

Fig. 13 shows the simulated signal of excited quark. The resonance shape at resonance masses of $M = 0.7, 1.2$, and 2.0 TeV are obtained from simulation. We obtain resonance shapes at intermediate masses via an interpolation technique [1], and at masses outside this interval via extrapolation using the same technique. The interpolation technique has been checked by doing a wider interpolating between $M = 0.7$ and 2.0 TeV to get the 1.2 TeV resonance and comparing that with the actual simulation, and the shapes were the same. We use the resonance shapes from our interpolation and extrapolation technique to calculate the cross section upper limit at any resonance mass.

Fig. 14 shows the differential cross section of excited quark signals as a function of dijet mass with background fit. CMS data based on 7.2 nb^{-1} is compared to the smooth background fit and to simulated resonance signals in Fig. 15.

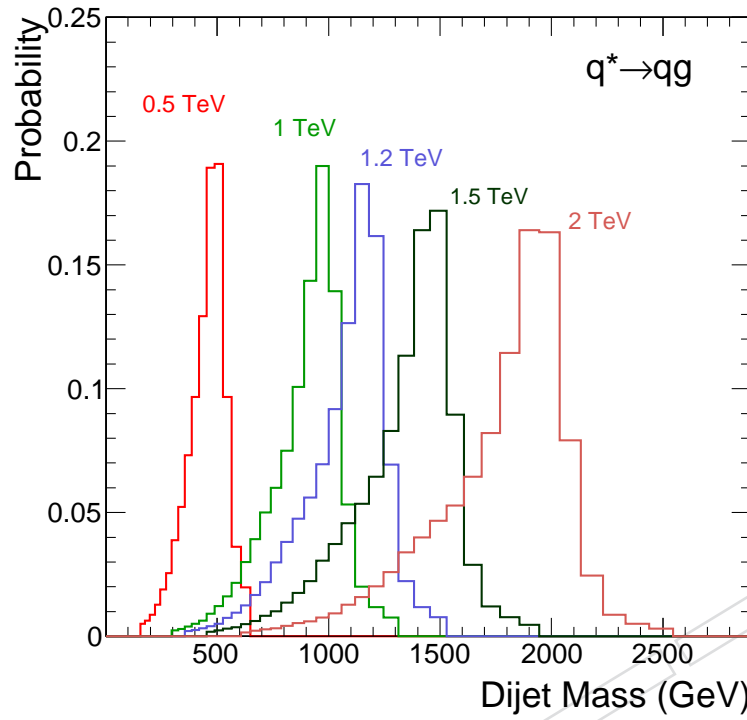


Figure 13: Resonance shapes at various resonance masses using interpolation technique.

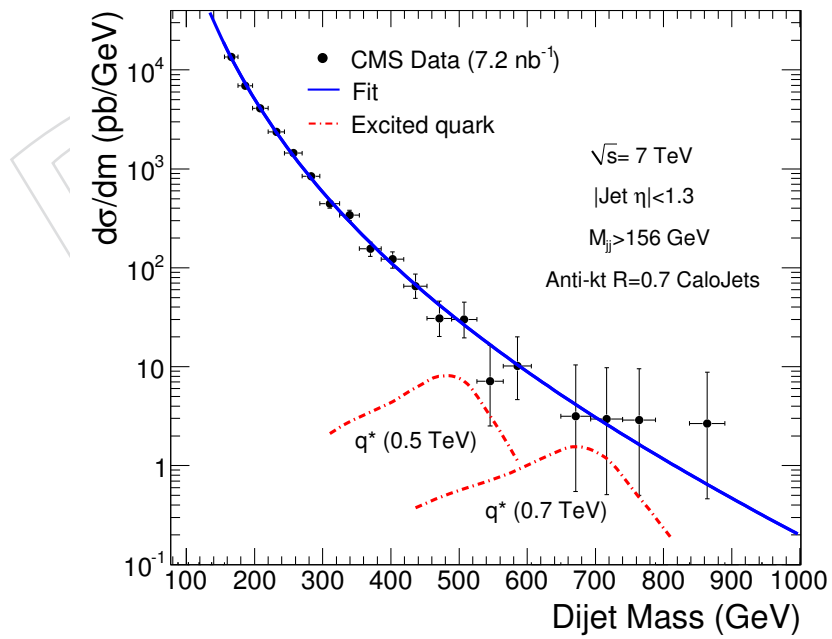


Figure 14: The dijet mass distribution (points) compared to a simulation of excited quarks signals in the CMS detector (dashed red curves).

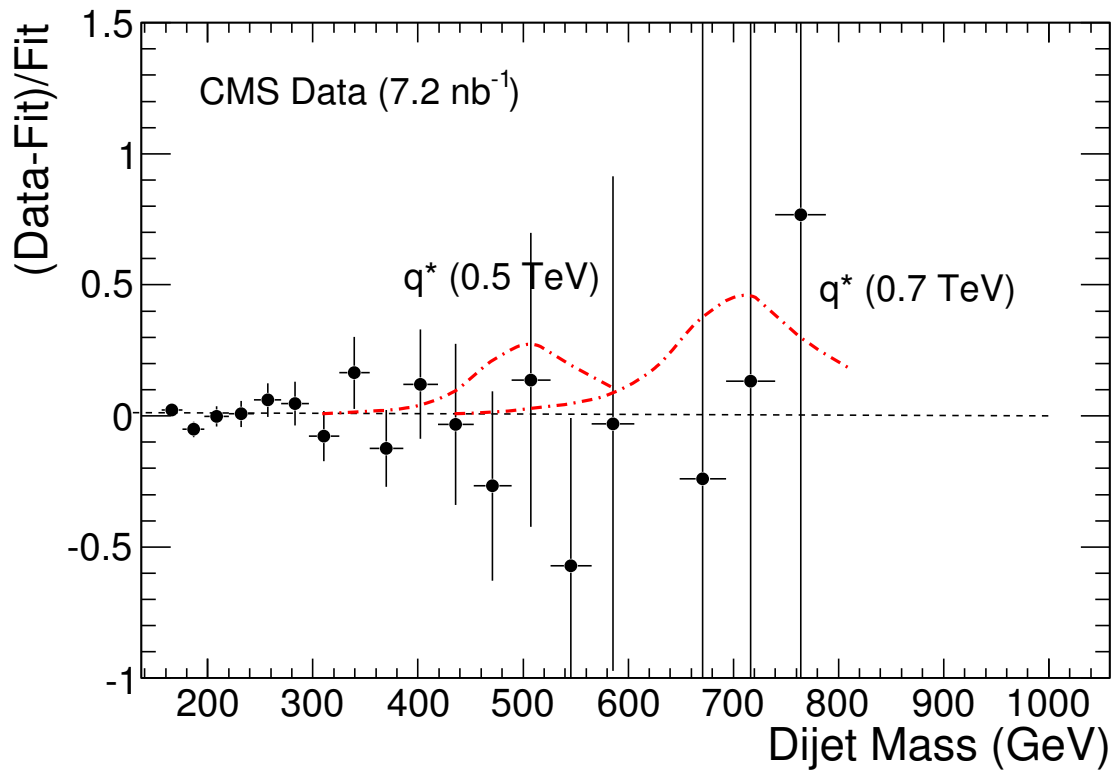


Figure 15: The fractional difference between the dijet mass distribution (points) and a smooth background fit (solid line) is compared to simulations of excited quark signals in the CMS detector (dashed red curves).

3.2 Largest Fluctuation and Significance

The search range of Dijet mass is not well defined since there is no prediction for the Dijet Resonance mass(es). Therefore the probability to find upward fluctuation is increased by searching for resonance(s) anywhere and we need to take the “Look Elsewhere Effect” into account. A MC simulation is used to estimate the significance of a resonance possibly to be observed in data. The biggest fluctuation in the current dataset (7.2 nb^{-1}) is used to illustrate the method.

Two fits to the data are defined as: the null-hypothesis fit is a fit to the data using background model only and the signal-hypothesis fit is a fit to the data using background model and a signal model together. The likelihood (χ^2) returned from the null- or signal-hypothesis fit is denoted as L_0 (χ_0^2) or L_S (χ_S^2). The $\sqrt{-2\Delta\ln} = \sqrt{-2\ln(L_0/L_S)}$ or $\sqrt{-\Delta\chi^2} = \sqrt{\chi_0^2 - \chi_S^2}$ value is called the local significance and will be used to determine the significance including the “Look Elsewhere Effect”. Fig. 16 and 17 show the null- and signal-hypothesis fit, with the lowest χ^2 at q^* mass of $270 \text{ GeV}/c^2$ in the search range of 200 to $800 \text{ GeV}/c^2$, to the current dataset (7.2 nb^{-1}) with a local significance of 1.7 obtained by $\sqrt{\Delta\chi^2} = \sqrt{2.83}$. And Fig. 18 shows the fractional background subtracted Dijet mass from the signal-hypothesis fit with a q^* fluctuation shape.

To estimate the probability that background fluctuations alone would give rise to signals (fluctuations) as significant as that seen in the data, we simulate Dijet mass spectra based on the background distribution alone, and search for the most significant fluctuation in each spectrum in the mass range of 200 to $800 \text{ GeV}/c^2$, with the q^* mass shape at various resonance masses. In this case, a total number of 4788 events (match to the total number of events in the data) is generated for each trial. From these simulated spectra we obtain the distribution for the quantity $-\Delta\chi^2$ in pure background samples, and compare this with the signal (fluctuation in this dataset) in the data. We performed a total of 100 and found 95 trials with a $-\Delta\chi^2$ value greater than or equal to the value obtained in the data as shown in Fig. 19. The p-value obtained from MC simulation is 95% , corresponding to a significance of 0σ . Thus, the significance is decreased from 1.7σ to 0σ by taking the “Look Elsewhere Effect” into account.

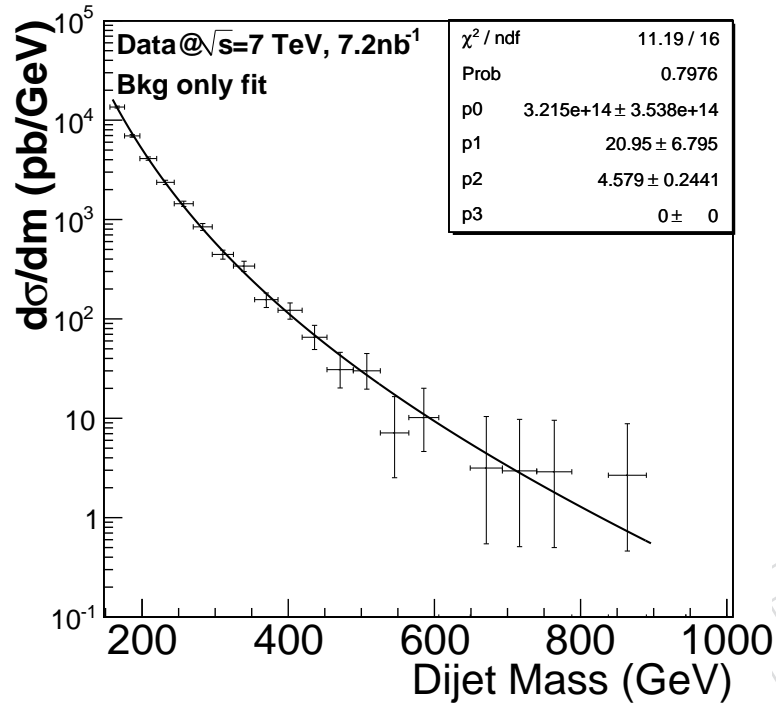


Figure 16: The null-hypothesis fit to the Dijet mass in the current dataset using equation 2.

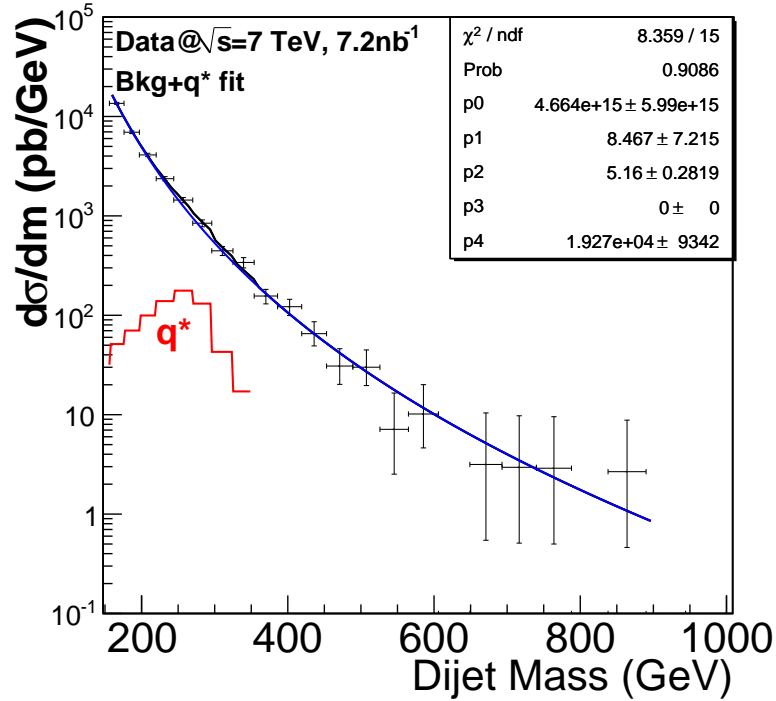


Figure 17: The signal-hypothesis fit to the Dijet mass in the current dataset using equation 2 and q^* resonance shape.

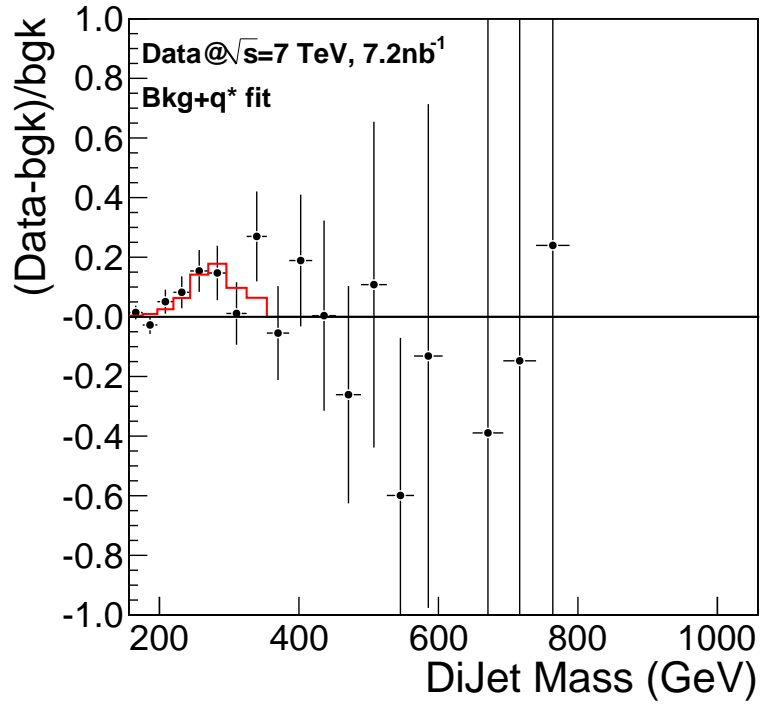


Figure 18: The fractional background subtracted Dijet mass from the signal-hypothesis fit.

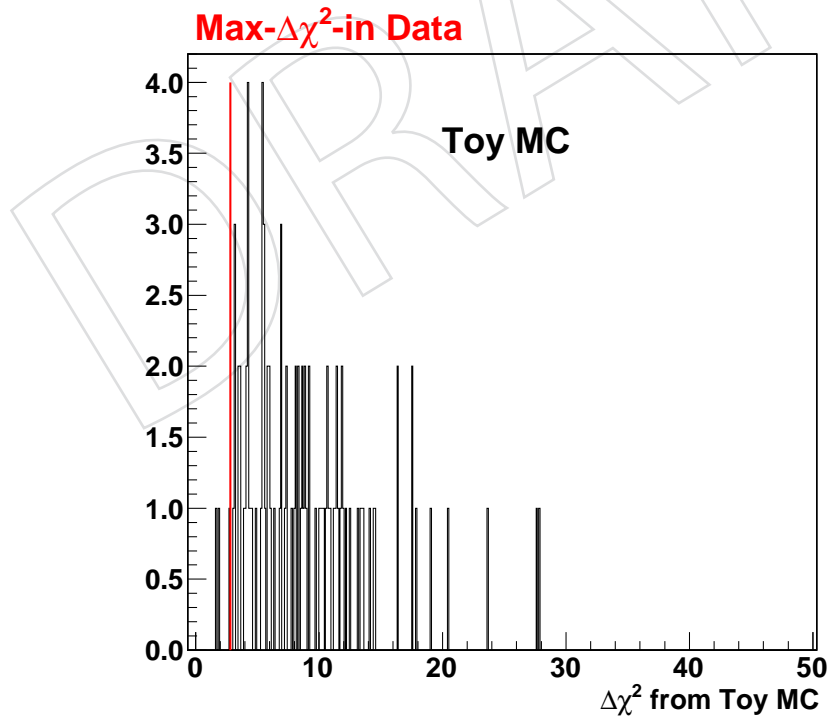


Figure 19: The $-\Delta\chi^2$ distribution obtained from MC simulation.

3.3 Setting Cross Section Upper Limits

Bayesian technique based on binned likelihood is used to calculate the limits on new particle production. The likelihood as a function of a constant can be written as:

$$L = \prod_i \frac{\mu_i^{n_i} e^{-\mu_i}}{n_i!} \quad (4)$$

where

$$\mu_i = \alpha N_i(S) + N_i(B). \quad (5)$$

n_i is measured number of events in the i -th dijet mass bin, $N_i(S)$ is number of events from signal in the i -th dijet mass bin, α is a constant to multiply the signal and $N_i(B)$ is number of expected events from background in the i -th dijet mass bin. We consider that QCD background is fixed to the best *Signal + QCD* fit to data point and it gives the expected number of background event in the i -th dijet mass bin, $N_i(B)$. The number of signal in the i -th dijet mass bin, $N_i(S)$, comes from developed interpolation technique. The signal range is chosen from $0.3 \cdot M_{Res}$ to $1.3 \cdot M_{Res}$ since high and low mass tail is affectively lost in QCD background. Then we plot likelihood distribution as a function of signal cross section for resonances with mass from $0.5 TeV$ to $1.5 TeV$ in $0.1 TeV$ steps, and the 95% confidence level upper limit is calculated as follows;

$$\frac{\int_0^{\sigma_{95}} L(\sigma) d\sigma}{\int_0^{\infty} L(\sigma) d\sigma} = 0.95 \quad (6)$$

We present 95% CL upper limit on Dijet resonance cross section in Fig. 20. Quark-quark, quark-gluon and gluon-gluon resonances are shown separately. Difference is small between different parton pair resonances.

Mass (TeV)	95% C.L. $\sigma \cdot B$ (pb) Stat. Err. Only		
	quark-quark	quark-gluon	gluon-gluon
0.5	1984	2375	3815
0.6	1085	1291	2113
0.7	1094	1177	1635
0.8	1023	1095	1384
0.9	828	893	1208
1.0	672	749	1015
1.1	591	647	856
1.2	542	588	723
1.3	503	535	671
1.4	473	503	612
1.5	458	480	593

Table 5: As a function of resonance mass we list our 95% C.L. upper limit on cross section times branching ratio for narrow resonances originating from o quark-quark, quark-gluon and gluon-gluon pairs of partons, including statistical errors only.

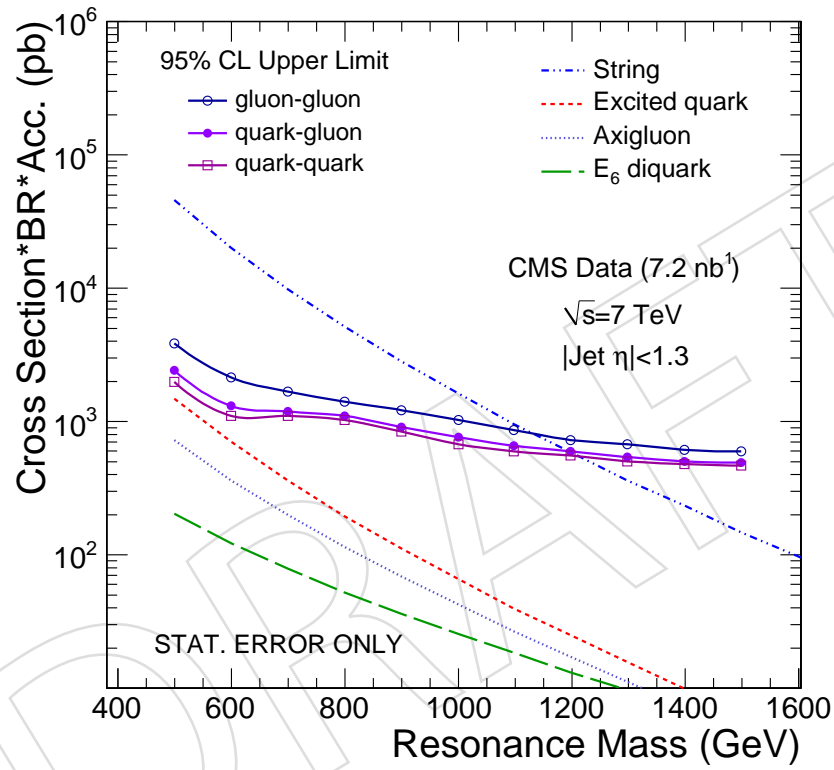


Figure 20: Dijet resonance sensitivity for 7.2 nb^{-1} CMS data. 95% C.L. is compared to the cross section for various resonance models. This sensitivity contains statistical error only.

4 Systematic Uncertainties

The source of systematic uncertainties are considered as following:

- Jet Energy Scale (JES)
- Jet Energy Resolution (JER)
- Choise of Background Parametrization
- Luminosity

4.1 Jet Energy Scale (JES)

The uncertainty on the JES that is important for this analysis is the uncertainty on how well the dijet resonance simulation models the jet energy scale of real jets. If the simulation produces jets with too high a response, then the true position of the expected resonance peak for that resonance mass would really be at lower mass than predicted by the simulation. We assume that the uncertainty on JES is roughly $\pm 10\%$ and test the sensitivity of our analysis to a shift in the resonance signal by 10%. Shifting the resonance 10% lower in dijet mass gives more background from QCD and finding the resonance signal is harder.

The left plot in Fig. 21 shows smooth cross section limit without systematics and with systematics on JES uncertainty for qg resonance. To get smooth cross section limit curve, expected events from background, $N_i(B)$, which is smooth and comes from fit function are considered as measurement number of events, n_i , in the i -th dijet mass bin. Fractional change between smooth limits are illustrated separately at right plot of Fig. 21. The uncertainty on JES varies roughly from 50% at 0.5 TeV to 10% at 1.5 TeV. The systematic uncertainty decreases with resonance mass primarily because we are setting limits at the edge of the region with real data, and the uncertainty is very sensitive to whether any data events are expected from the background: if there is no background, there is no change in the limit with JES uncertainty. This systematic has increased with luminosity at high resonance mass, and we expect that this systematic uncertainty will continue to increase as we get more data.

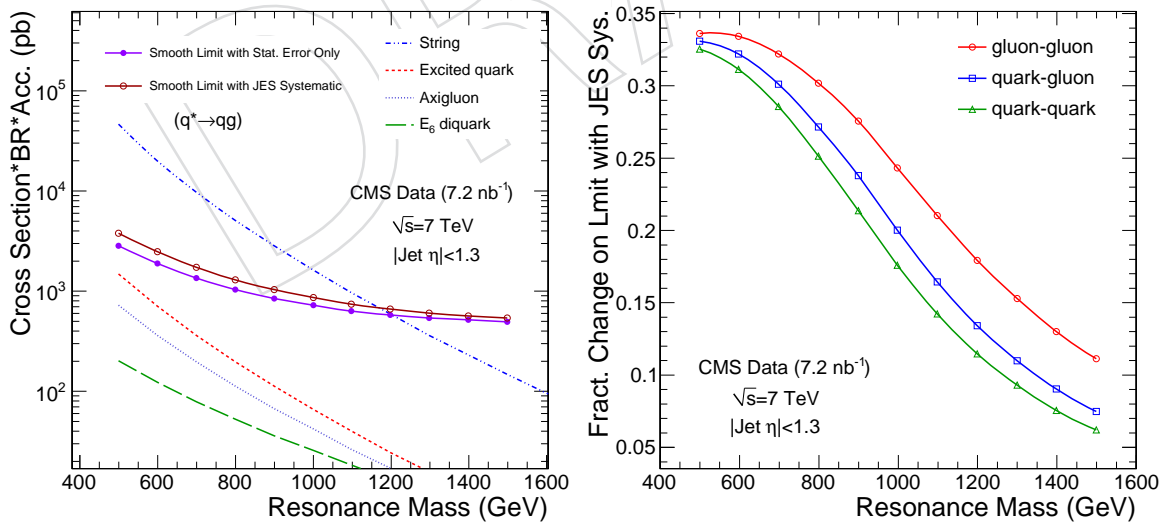


Figure 21: *Left plot:* Comparison of smoothed cross section limit without systematics and with systematic on JES uncertainty. *Right plot:* Fractional change on limit with JES systematic uncertainty.

4.2 Jet Energy Resolution (JER)

We assume that the uncertainty on JER is roughly $\pm 10\%$ and the signal is being smeared with a gaussian that increases the core resolution by 10%. A comparison of resonance shapes are shown in Fig.22.

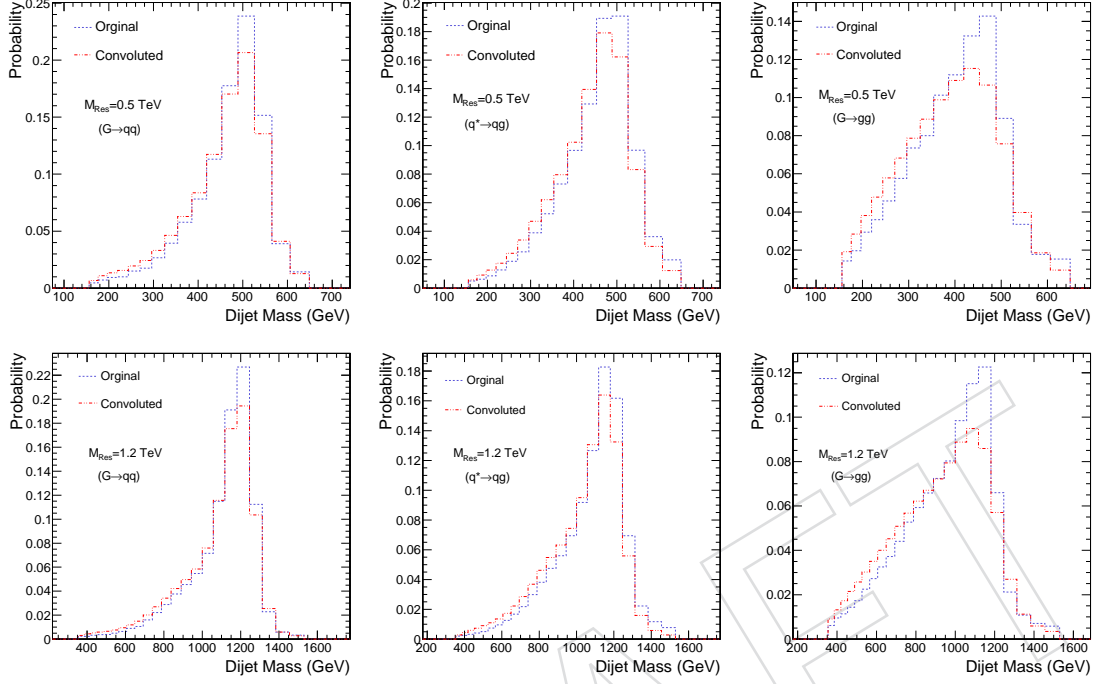


Figure 22: Resonance shape comparison after convolution at 0.5 GeV (top) and 1.2 TeV (bottom).

Dijet mass core resolution of the resonance signal as a function of resonance mass was illustrated in Fig. 12. The resolution is calculated as Sigma/Mean which are obtained from gaussian fit of dijet mass distribution. The fractional change on Limit with JER systematic is illustrated in Fig. 23. Effect of resolution uncertainty on limit is small.

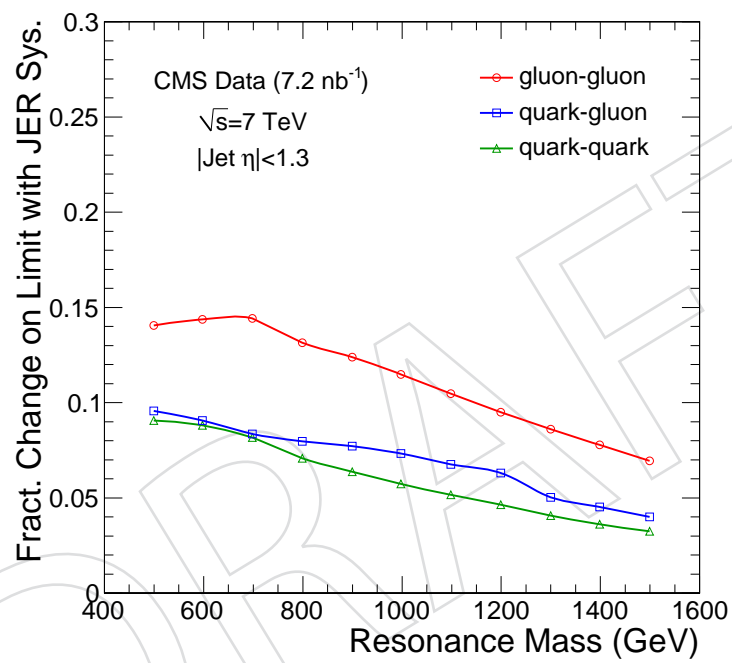


Figure 23: Fractional change on limit with JER systematic uncertainty.

4.3 Background Parameterization

We considered two others functional forms with 2 and 4 parameters to parameterize the QCD background as discussed in section ?? and shown in Equation 3. Fig. 24 show comparison of fits with the data points. We find taht the 2 parameter form, which is a marginal fit to our data, gives the largest fractional change over the vsat majority of resonance masses, and we conservatively use it for our background parametrization systematic at this time.

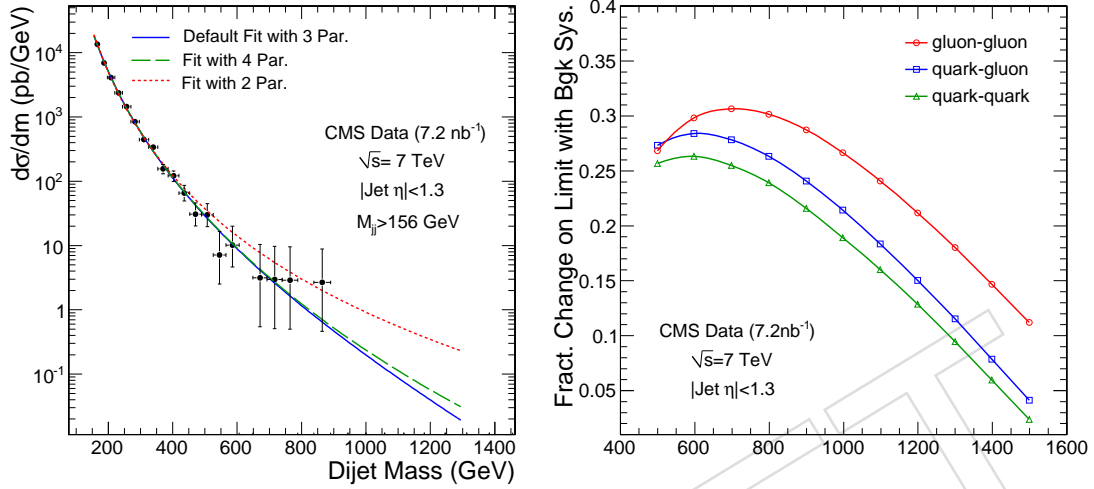


Figure 24: Left) The data and the default 3 parameter fit and the 2 and 4 parameter fits use to evaluate the systematics. Right) Fractional absolute change in the limit when using th 2 and 4 parameter fits for the background.

4.4 Total Uncertainty

We determine 1σ change for each systematic uncertainty in signal that we can discovery or exclude. In addition to the sources already mentinoned, we include an uncertainty of 10% on the integrated luminosity.

To find total total systematics, we add the these 1σ changes as quadrature. The individual and total systematic uncertainties as a function of resonance mass are illustrated in Fig. 25. Absolute uncertainty in each resonance mass is calculated as total systematics uncertainty multiply by upper cross section limit.

The same procedure is repeated for qq and gg resonance shapes to get systematics for those, yielding similar systematic uncertainties.

4.5 Incorporating Systematics in the Limit

We convolute likelihood distribution with gaussian for each resonance mass. The width of gaussian is taken as absolute uncertainty in each resonance mass. The equation of convolution is taken as following

$$L(\vartheta) = \int_0^\infty L(\sigma)G(\sigma)d\sigma \quad (7)$$

Likelihood distributions with systematic uncertainties is shown in Appendix D. Total likelihood including systematics is broader and gives higher upper limit. 95% CL Upper limit with

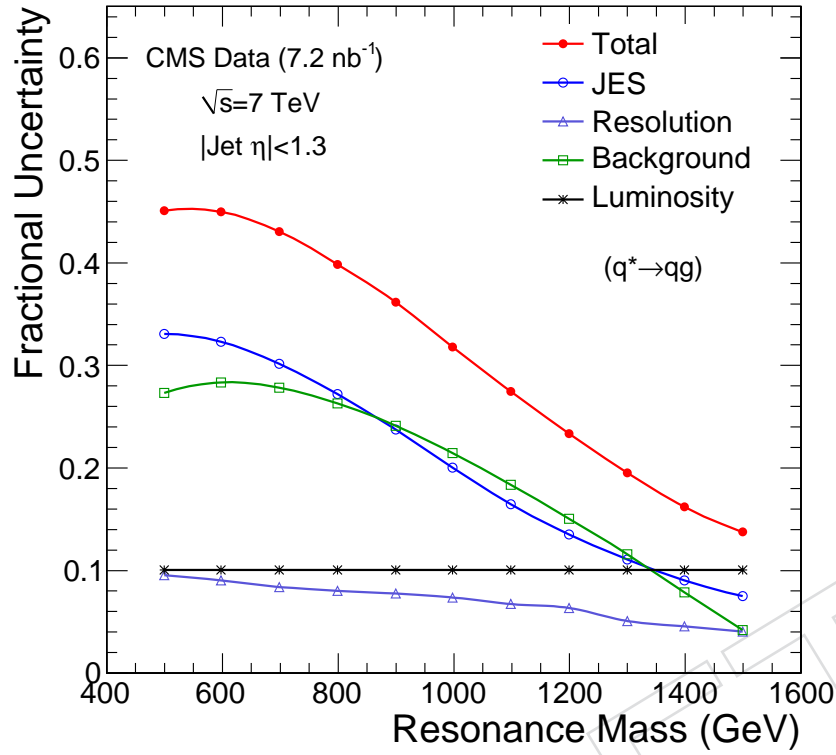


Figure 25: Fractional systematic uncertainties on signal cross section.

383 Stat. Error. Only and Including Sys. Uncertainties are shown separately in Fig. 26. The ef-
 384 fects of systematics is presented Fig. 26. Cross section limits increase by about 50% - 10% with
 385 systematics uncertainties.

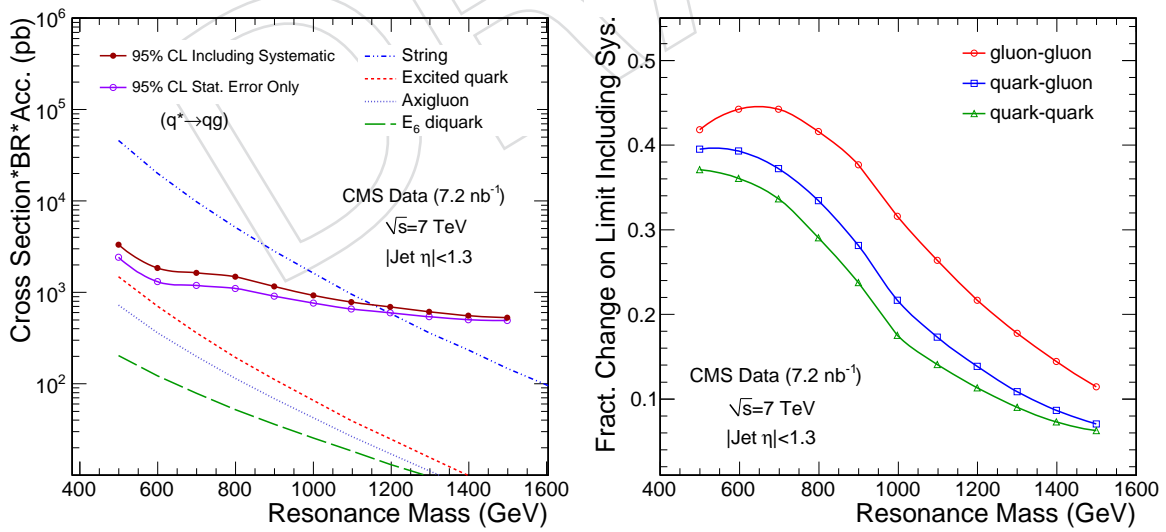


Figure 26: Left) Limits on qq resonances with and without all systematic uncertainties. Right) Fractional change in the limit after including systematics.

5 Results

Our 95% CL limits on the cross section for narrow dijet resonances are shown in Fig 27 and listed in Table 6. These are limits on the cross section, times branching ratio for decay to dijets, times acceptance for the fiducial cut $|\eta| < 1.3$. Separate limits are shown for the three different parton pairs qq , qg and gg which have different resonance shapes. The limits are compared with calculations of the cross section times branching ratio for dijets with the $|\eta| < 1.3$ cut from three different models: Excited Quarks, Axigluons (or Colorons), and E_6 diquarks. The 95% CL upper limit on the cross section is above the model cross sections, so we do not constrain the mass of any of these models with this data sample.

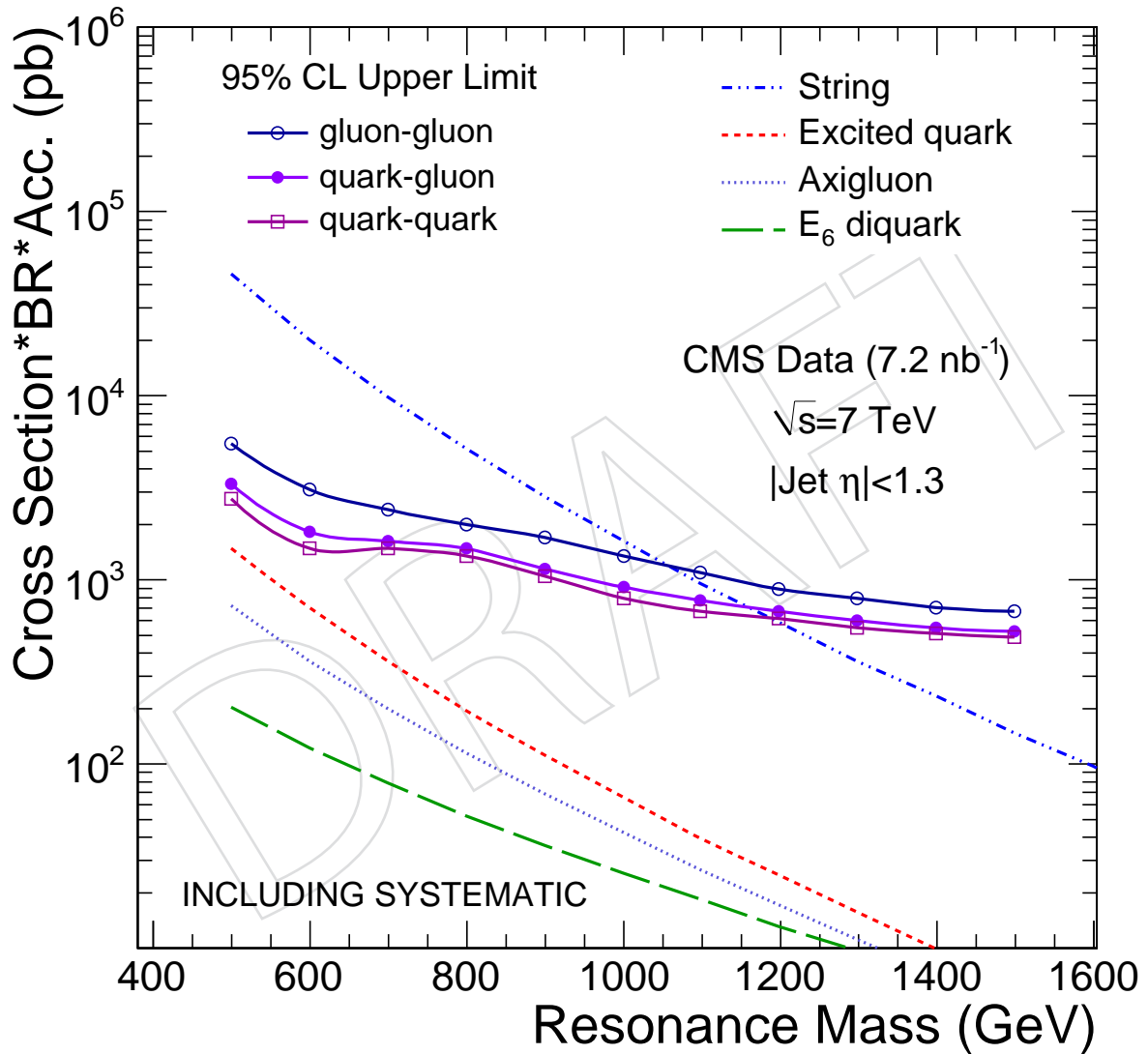


Figure 27: The 95% CL upper limits on the cross section for dijet resonances (points) shown separately for the three different parton pairs qq , qg and gg , is compared to the model cross section for Excited Quarks, Axigluons (or Colorons) and E_6 diquarks.

Mass (TeV)	95% C.L. $\sigma \cdot B$ (pb)		
	quark-quark	quark-gluon	gluon-gluon
0.5	2719	3312	5410
0.6	1476	1797	3047
0.7	1462	1615	2357
0.8	1320	1460	1959
0.9	1024	1144	1662
1.0	790	911	1335
1.1	674	759	1081
1.2	603	669	880
1.3	548	593	790
1.4	508	546	700
1.5	487	514	660

Table 6: As a function of resonance mass we list our 95% C.L. upper limit on cross section times branching ratio for narrow resonances originating from quark-quark, quark-gluon, and gluon-gluon pairs of partons, including systematic uncertainties.

395 .mine

396 6 Expected Future Limits

397 We have used the methodology described in this note and in a prior analysis [1] to determine
 398 our expected limits with more integrated luminosity. For the expected limits the PYTHIA MC
 399 samples discussed previously were used for the background, but otherwise the analysis is the
 400 same as just described. We form smooth samples background samples without fluctuations
 401 from a smooth fit to the QCD data and use the number of events expected in each bin from this
 402 smooth fit to perform the analysis. The expected upper limits on the cross section are shown
 403 in Fig. 30 compared to 6 models of resonance. The mass limit expected for each model occurs
 404 where the expected upper limit on the cross section for the appropriate parton pair crosses the
 405 model cross section curve. These expected 95% CL mass limits are tabulated in table 8 as a
 406 function of integrated luminosity and plotted in Figure 31. From a linear fit to the expected
 407 mass limit as a function of the logarithm of the integrated luminosity, we find that with 400
 408 nb^{-1} we expect to reach the mass limit of 870 GeV for excited quarks set by the Tevatron.

Model Name	95% C.L. Excluded Mass (TeV)					
	0.1 pb^{-1}	0.3 pb^{-1}	1 pb^{-1}	10 pb^{-1}	100 pb^{-1}	1 fb^{-1}
Excited Quark	0.59	0.82	1.06	1.55	2.05	2.55
Axigluon/Cloloron	N/A	0.64	0.95	1.51	2.07	2.57
Excited Quark	N/A	N/A	N/A	1.60	2.44	3.10

Table 7: 95% C.L. Excluded Mass for various model

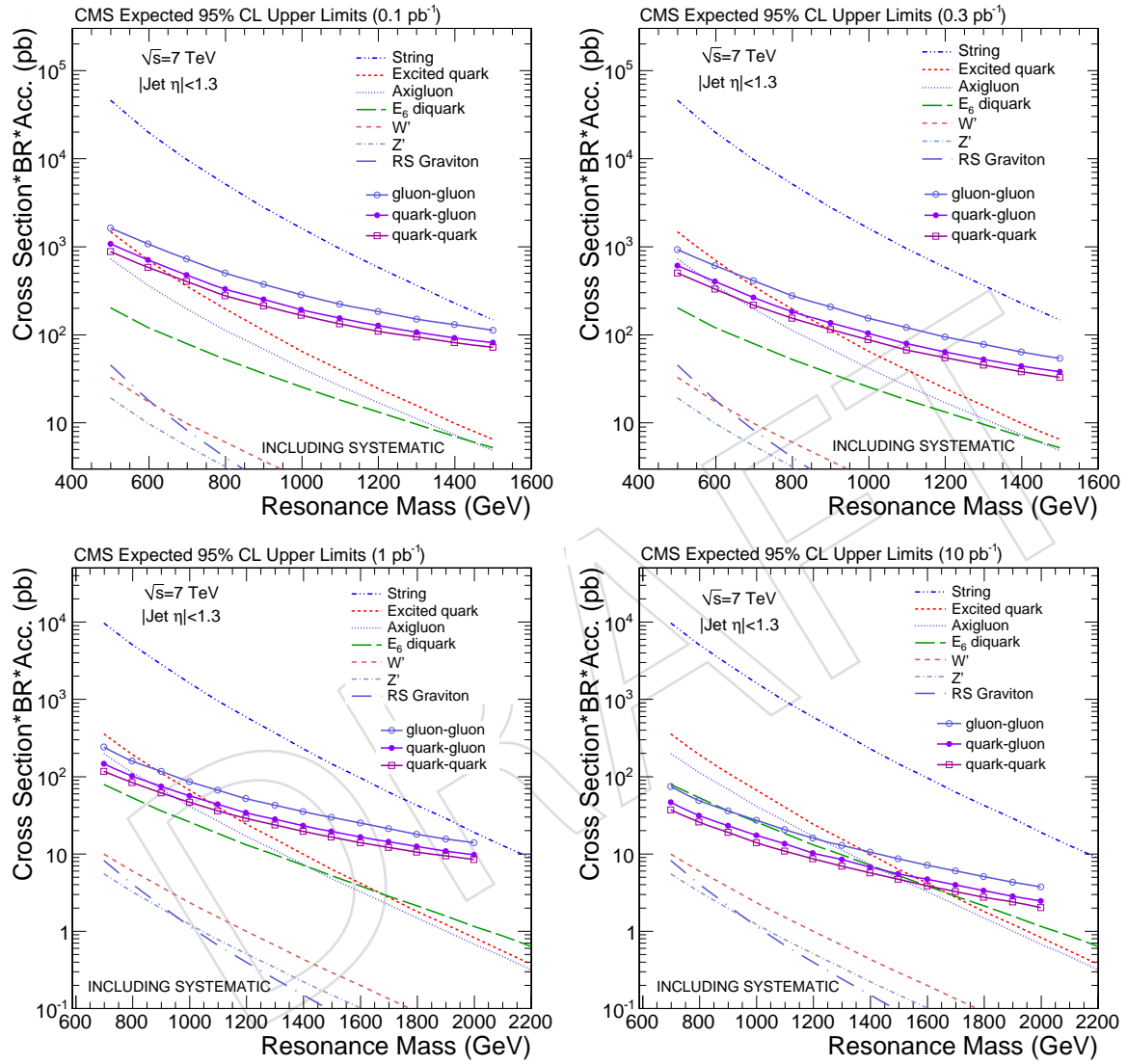


Figure 28: Dijet Resonance Sensitivities of CMS detector

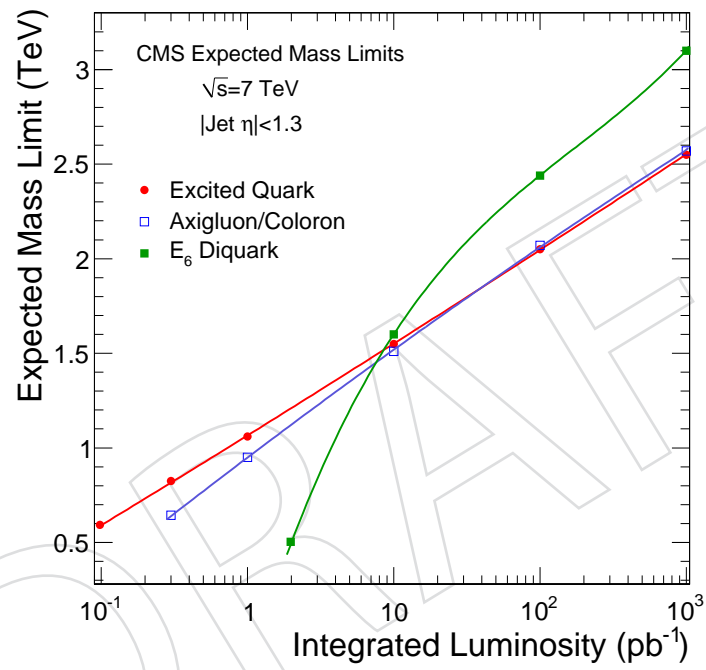


Figure 29: Excluded Mass limits

409 =====

410 7 Expected Future Limits

411 We have used the methodology described in this note and in a prior analysis [1] to determine
 412 our expected limits with more integrated luminosity. For the expected limits the PYTHIA MC
 413 samples discussed previously were used for the background, but otherwise the analysis is the
 414 same as just described. We form smooth samples background samples without fluctuations
 415 from a smooth fit to the QCD data and use the number of events expected in each bin from this
 416 smooth fit to perform the analysis. The expected upper limits on the cross section are shown
 417 in Fig. 30 compared to 6 models of resonance. The mass limit expected for each model occurs
 418 where the expected upper limit on the cross section for the appropriate parton pair crosses the
 419 model cross section curve. These expected 95% CL mass limits are tabulated in table 8 as a
 420 function of integrated luminosity and plotted in Figure 31. From a linear fit to the expected
 421 mass limit as a function of the logarithm of the integrated luminosity, we find that with 400
 422 nb^{-1} we expect to reach the mass limit of 870 GeV for excited quarks set by the Tevatron.

Model Name	95% C.L. Excluded Mass (TeV)					
	0.1 pb^{-1}	0.3 pb^{-1}	1 pb^{-1}	10 pb^{-1}	100 pb^{-1}	1 fb^{-1}
Excited Quark	0.59	0.82	1.06	1.55	2.05	2.55
Axigluon/Cloloron	N/A	0.64	0.95	1.51	2.07	2.57
Excited Quark	N/A	N/A	N/A	1.60	2.44	3.10

Table 8: 95% C.L. Excluded Mass for various model

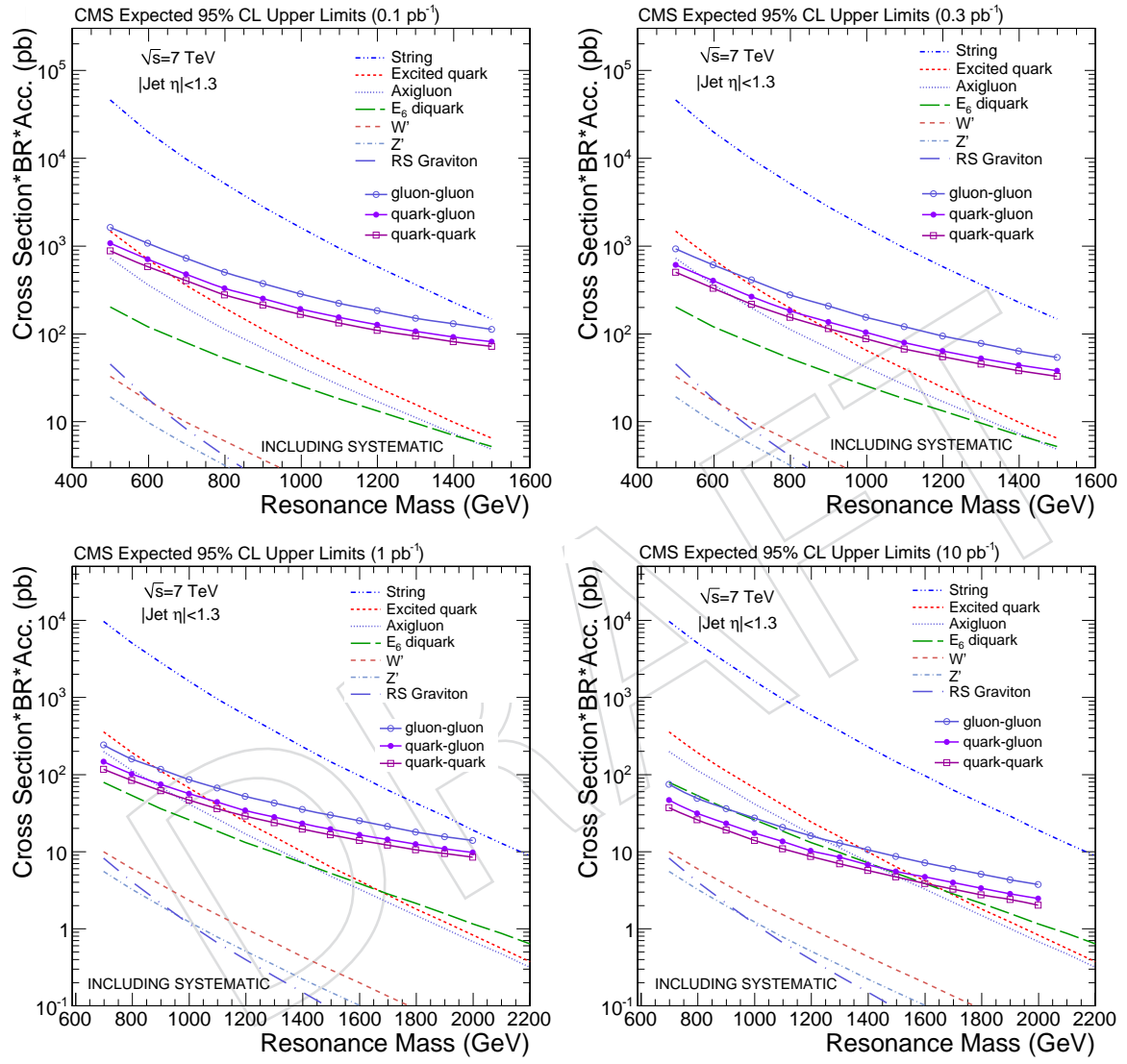


Figure 30: Dijet Resonance Sensitivities of CMS detector

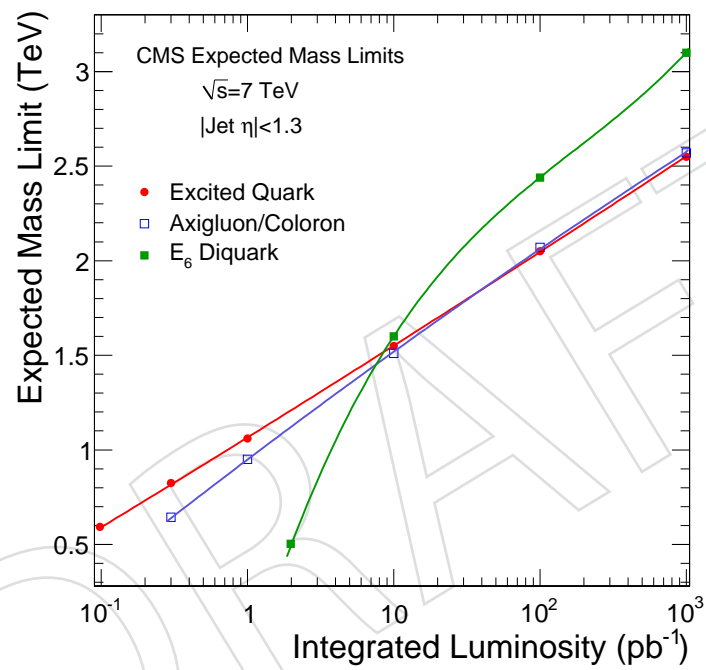


Figure 31: Excluded Mass limits

423 `../../../../r6701`

424 8 Conclusions

425 We have used 7.2 nb^{-1} of CMS data to measure the dijet mass spectrum in the region $|\eta| < 1.3$.
 426 The event with the largest observed dijet mass is at $m = 851 \text{ GeV}$. The measured dijet mass
 427 spectrum is in good agreement with a QCD prediction from PYTHIA and the full simulation
 428 of the CMS detector.

429 We have performed direct searches for high-mass dijet resonances in the dijet mass distribution.
 430 The dijet mass data is well fit by a simple parameterization with three parameters. There is no
 431 significant evidence for new particle production in the data. We set 95% confidence level upper
 432 limits on the cross section for a dijet resonance, applicable to any narrow resonance producing
 433 the following specific pairs of partons: qq , qg , and gg . We have compared our cross section
 434 limits with the expected cross sections from several existing models. The limits are all greater
 435 than the predicted cross sections, so we cannot constrain the mass of these models yet. With
 436 0.1 pb^{-1} we anticipate being able to exclude excited quarks with a mass of 590 GeV , and with
 437 0.4 pb^{-1} we anticipate reaching the Tevatron exclusion of 870 GeV .

DRAFT

A Resonance Model Cross Sections

Mass (GeV)	q^* (pb)	A or C (pb)	D (pb)	Z' (pb)	W' (pb)	G (pb)
500.0	0.1472E+04	0.7155E+03	0.1993E+03	0.1884E+02	0.3248E+02	0.4516E+02
600.0	0.6940E+03	0.3584E+03	0.1210E+03	0.9749E+01	0.1729E+02	0.1816E+02
700.0	0.3562E+03	0.1950E+03	0.7789E+02	0.5435E+01	0.9874E+01	0.8186E+01
800.0	0.1942E+03	0.1123E+03	0.5219E+02	0.3191E+01	0.5913E+01	0.4016E+01
900.0	0.1107E+03	0.6731E+02	0.3597E+02	0.1944E+01	0.3663E+01	0.2101E+01
1000.0	0.6529E+02	0.4158E+02	0.2531E+02	0.1218E+01	0.2325E+01	0.1156E+01
1100.0	0.3956E+02	0.2627E+02	0.1808E+02	0.7793E+00	0.1504E+01	0.6618E+00
1200.0	0.2449E+02	0.1689E+02	0.1306E+02	0.5069E+00	0.9858E+00	0.3913E+00
1300.0	0.1542E+02	0.1101E+02	0.9522E+01	0.3339E+00	0.6528E+00	0.2374E+00
1400.0	0.9852E+01	0.7258E+01	0.6986E+01	0.2223E+00	0.4356E+00	0.1471E+00
1500.0	0.6370E+01	0.4826E+01	0.5151E+01	0.1492E+00	0.2922E+00	0.9273E-01
1600.0	0.4159E+01	0.3231E+01	0.3811E+01	0.1008E+00	0.1967E+00	0.5929E-01
1700.0	0.2738E+01	0.2176E+01	0.2827E+01	0.6847E-01	0.1327E+00	0.3835E-01
1800.0	0.1816E+01	0.1472E+01	0.2100E+01	0.4670E-01	0.8961E-01	0.2505E-01
1900.0	0.1211E+01	0.9988E+00	0.1562E+01	0.3196E-01	0.6049E-01	0.1648E-01
2000.0	0.8122E+00	0.6795E+00	0.1161E+01	0.2192E-01	0.4079E-01	0.1092E-01
2100.0	0.5468E+00	0.4631E+00	0.8633E+00	0.1506E-01	0.2745E-01	0.7264E-02
2200.0	0.3694E+00	0.3160E+00	0.6411E+00	0.1035E-01	0.1842E-01	0.4852E-02
2300.0	0.2502E+00	0.2156E+00	0.4753E+00	0.7118E-02	0.1231E-01	0.3249E-02
2400.0	0.1698E+00	0.1470E+00	0.3517E+00	0.4891E-02	0.8196E-02	0.2180E-02
2500.0	0.1154E+00	0.1002E+00	0.2596E+00	0.3356E-02	0.5428E-02	0.1463E-02
2600.0	0.7850E-01	0.6811E-01	0.1910E+00	0.2298E-02	0.3574E-02	0.9819E-03
2700.0	0.5342E-01	0.4619E-01	0.1401E+00	0.1569E-02	0.2339E-02	0.6582E-03
2800.0	0.3635E-01	0.3123E-01	0.1023E+00	0.1067E-02	0.1520E-02	0.4404E-03
2900.0	0.2472E-01	0.2103E-01	0.7444E-01	0.7232E-03	0.9803E-03	0.2939E-03
3000.0	0.1679E-01	0.1410E-01	0.5389E-01	0.4876E-03	0.6272E-03	0.1954E-03
3100.0	0.1139E-01	0.9398E-02	0.3881E-01	0.3269E-03	0.3978E-03	0.1294E-03
3200.0	0.7715E-02	0.6227E-02	0.2779E-01	0.2177E-03	0.2500E-03	0.8518E-04
3300.0	0.5214E-02	0.4098E-02	0.1977E-01	0.1440E-03	0.1557E-03	0.5575E-04
3400.0	0.3515E-02	0.2676E-02	0.1398E-01	0.9445E-04	0.9596E-04	0.3623E-04
3500.0	0.2364E-02	0.1733E-02	0.9809E-02	0.6141E-04	0.5858E-04	0.2336E-04
3600.0	0.1585E-02	0.1111E-02	0.6830E-02	0.3955E-04	0.3541E-04	0.1493E-04
3700.0	0.1059E-02	0.7055E-03	0.4716E-02	0.2520E-04	0.2119E-04	0.9452E-05
3800.0	0.7059E-03	0.4430E-03	0.3227E-02	0.1587E-04	0.1257E-04	0.5920E-05
3900.0	0.4687E-03	0.2749E-03	0.2186E-02	0.9880E-05	0.7398E-05	0.3666E-05
4000.0	0.3102E-03	0.1684E-03	0.1466E-02	0.6069E-05	0.4321E-05	0.2243E-05
4100.0	0.2046E-03	0.1018E-03	0.9714E-03	0.3679E-05	0.2510E-05	0.1354E-05

Table 9: Cross section for dijet resonances in pp collisions at $\sqrt{s} = 7$ TeV with jet pseudorapidity $|\eta| < 1.3$. The models are Excited Quark (q^*), Axigluon or Coloron (A or C), E_6 diquark (D), Z' , W' and Randall-Sundrum Graviton (G). Lowest order calculation described previously [3]

B Binning and Data Table

The lower edges of the dijet mass bins, in GeV, are 1, 3, 6, 10, 16, 23, 31, 40, 50, 61, 74, 88, 103, 119, 137, 156, 176, 197, 220, 244, 270, 296, 325, 354, 386, 419, 453, 489, 526, 565, 606, 649, 693, 740, 788, 838, 890, 944, 1000, 1058, 1118, 1181, 1246, 1313, 1383, 1455, 1530, 1607, 1687, 1770, 1856, 1945, 2037, 2132, 2231, 2332, 2438, 2546, 2659, 2775, 2895, 3019, 3147, 3279, 3416, 3558, 3704, 3854, 4010. Table 10 shows the data observed with this binning above our dijet mass cut for full trigger efficiency.

Low Edge (GeV)	Bin Width (GeV)	Evts	$d\sigma/dm$ (pb/GeV)	Stat. Err. (pb/GeV)
156	20	1951	13363	302.535
176	21	1050	6849.31	211.374
197	23	680	4050.03	155.312
220	24	409	2334.47	115.432
244	26	270	1422.55	86.5736
270	26	158	832.455	66.2266
296	29	93	439.301	45.5534
325	29	71	335.38	39.8023
354	32	36	154.11	25.6849
386	33	29	120.382	22.3544
419	34	16	64.4641	16.116
453	36	8	30.4414	10.7627
489	37	8	29.6187	10.4718
526	39	2	7.02494	4.96738
565	41	3	10.0234	5.78701
606	43	0	0	0
649	44	1	3.11333	3.11333
693	47	1	2.9146	2.9146
740	48	1	2.85388	2.85388
788	50	0	0	0
838	52	1	2.63435	2.63435
890	54	0	0	0
944	56	0	0	0
1000	58	0	0	0
1058	60	0	0	0
1118	63	0	0	0
1181	65	0	0	0
1246	67	0	0	0
1313	70	0	0	0

Table 10: For each bin of dijet mass data we list the lower bin edge, the bin width, the number of events, the observed differential cross section, and an estimate of the statistical uncertainty from Gaussian statistics.

446

C Event Displays of High Mass Dijet Events

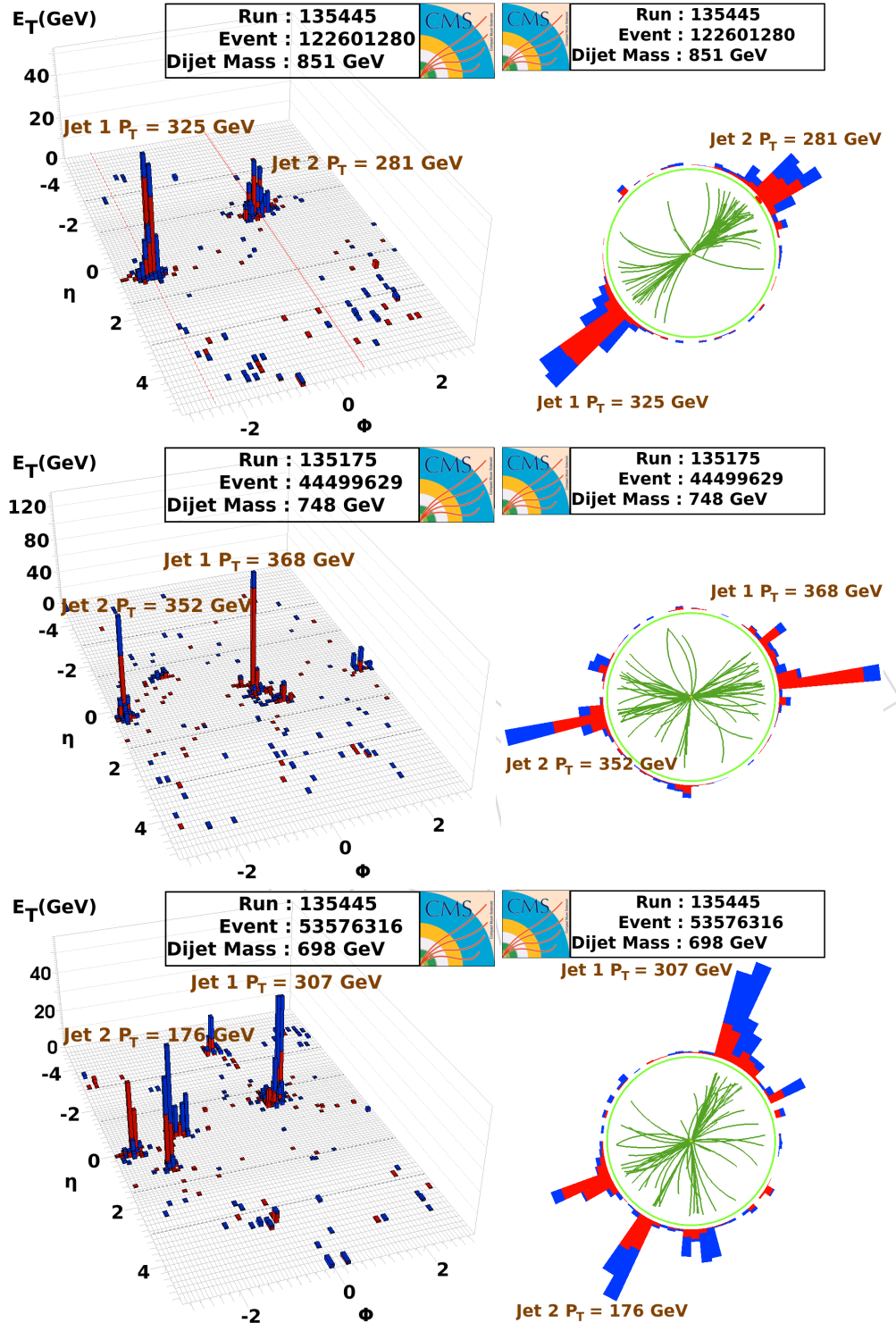


Figure 32: Lego (left) and $\rho - \phi$ (right) displays of the 1st to 3rd Highest Masss Dijet Events

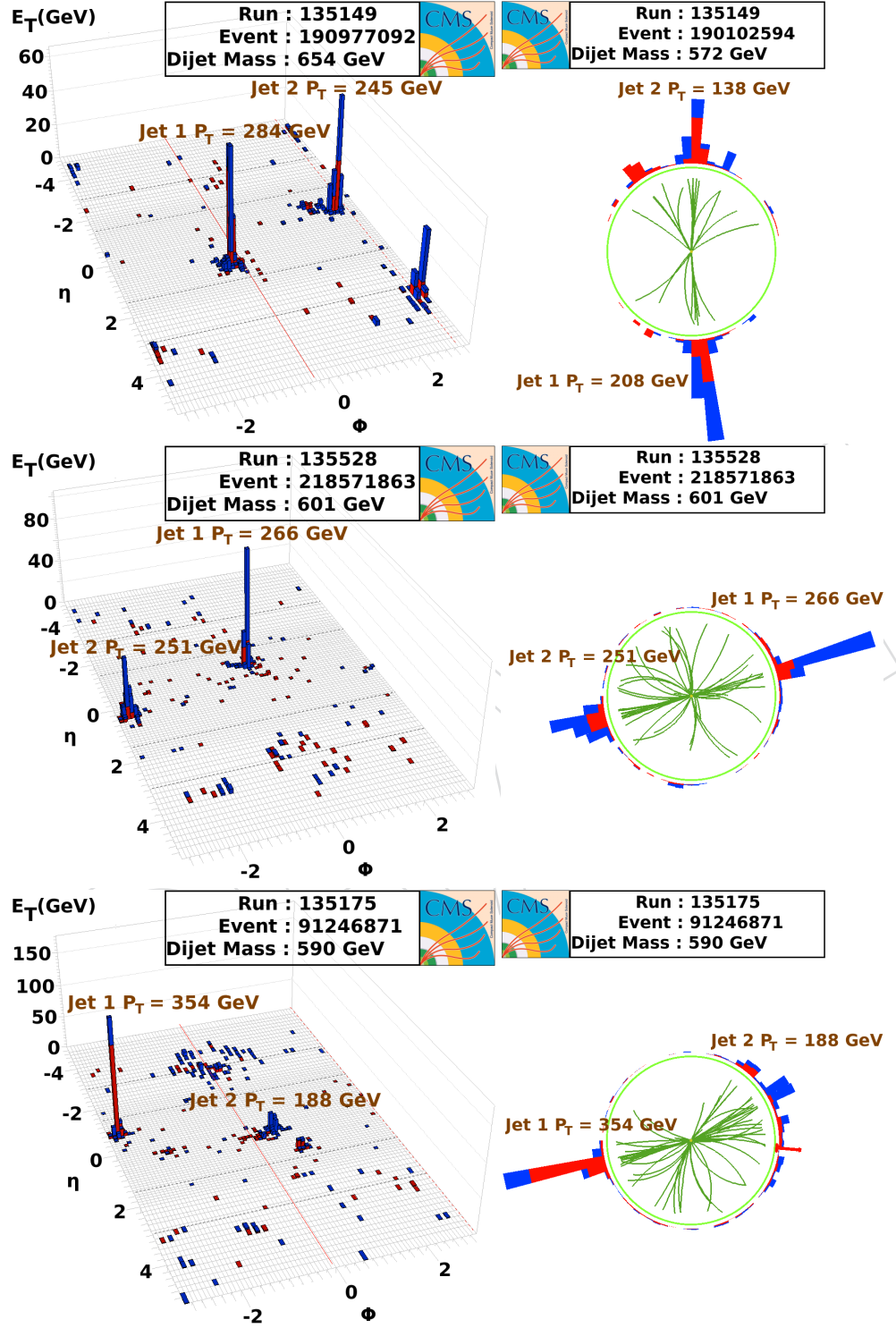
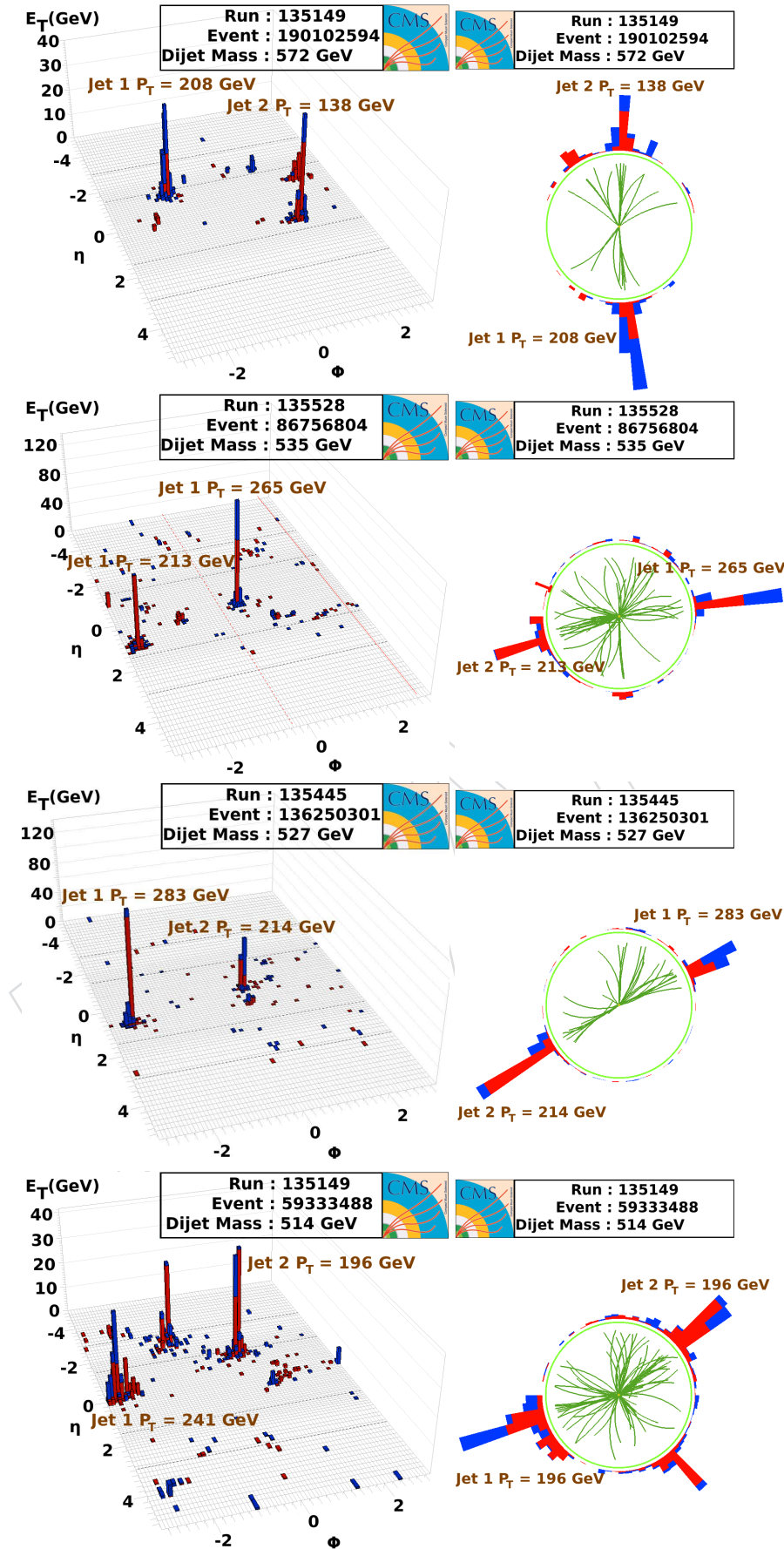


Figure 33: Lego (left) and $\rho - \phi$ (right) displays of the 4th to 6th Highest Masss Dijet Events

Figure 34: Lego (left) and $\rho - \phi$ (right) displays of the 7th to 10th Highest Mass Dijet Events

<i>Run</i>	<i>Event</i>	<i>DijetMass(GeV)</i>	<i>ME_T/SumE_T</i>
135445	122601280	851	0.11
135175	44499629	748	0.00
135445	53576316	698	0.02
135149	190977092	654	0.08
135528	218571863	601	0.04
135175	91246871	590	0.08
135149	190102594	572	0.05
135528	86756804	535	0.09
135445	136250301	527	0.09
135149	59333488	514	0.06

Table 11: Dijet Mass and $ME_T/SumE_T$

<i>Run</i>	<i>Event</i>	<i>Jet 1 CorP_T(GeV)</i>	<i>Jet 1 η</i>	<i>Jet 1 ϕ</i>	<i>Jet 2 CorP_T(GeV)</i>	<i>Jet 2 η</i>	<i>Jet 2 ϕ</i>
135445	122601280	325	0.7	-2.5	281	-1.1	0.7
135175	44499629	368	0.5	0.3	352	0.3	-3.0
135445	53576316	307	-1.1	1.1	176	0.8	-2.1
135149	190977092	284	0.9	-0.6	245	-0.4	2.5
135528	218571863	266	-0.7	0.3	251	0.4	-2.9
135175	91246871	354	-0.7	-2.9	188	0.3	0.5
135149	190102594	208	-1.2	-1.5	138	1.0	1.5
135528	86756804	265	0.1	0.2	213	1.1	-2.9
135445	136250301	283	0.7	-2.6	214	-0.0	0.5
135149	593334884	241	-0.1	-2.8	197	-1.3	0.7

Table 12: Dijet properties (corrected P_T , η and ϕ)

447 D Likelihood Distributions

DRAFT

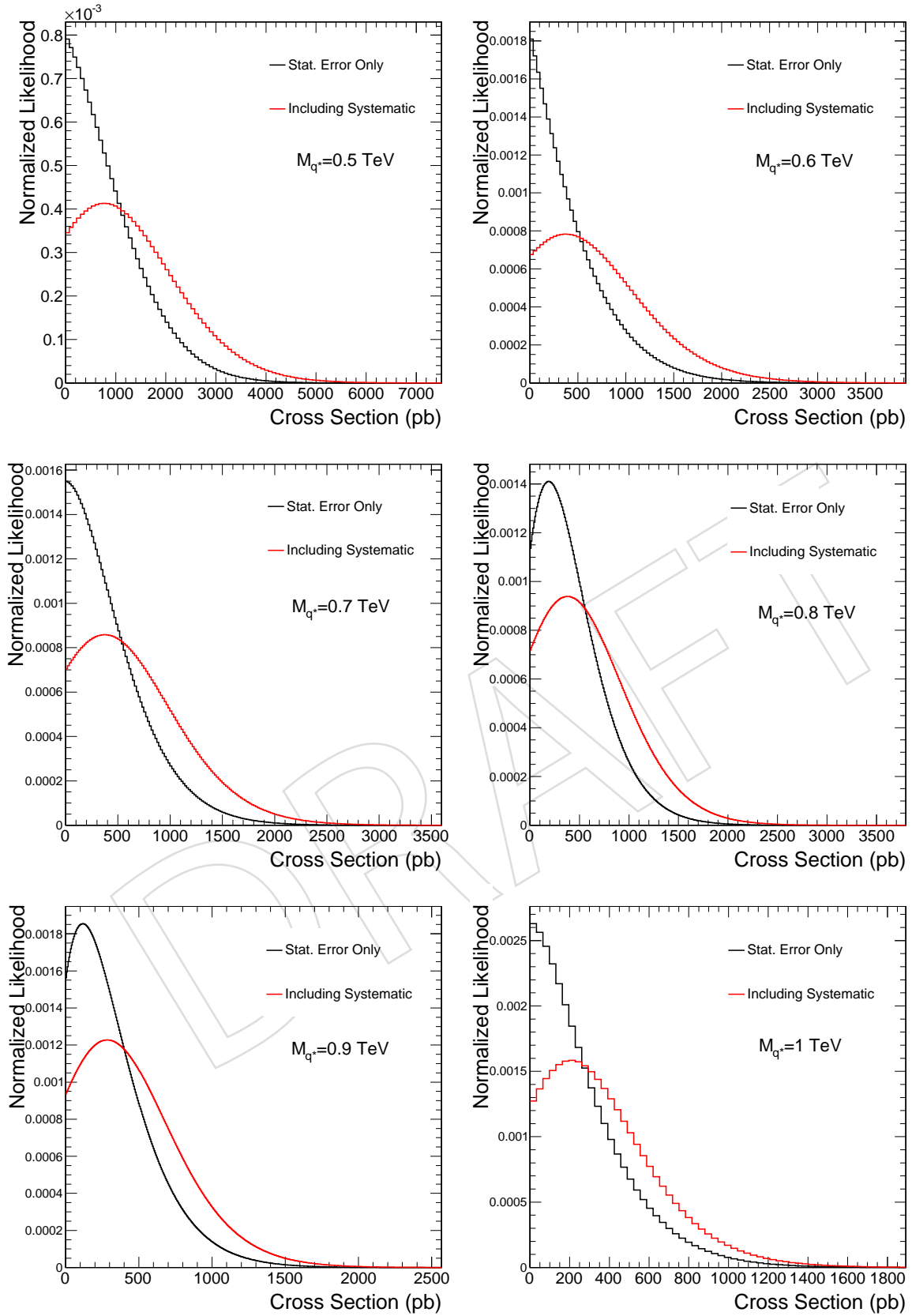


Figure 35: Likelihood distribution with %95 C.L. cross section limit at various excited quark resonance masses including systematics. Black line is %95 C.L. cross section limit with statistical error only. Red line shows %95 C.L. cross section limit with including systematics.

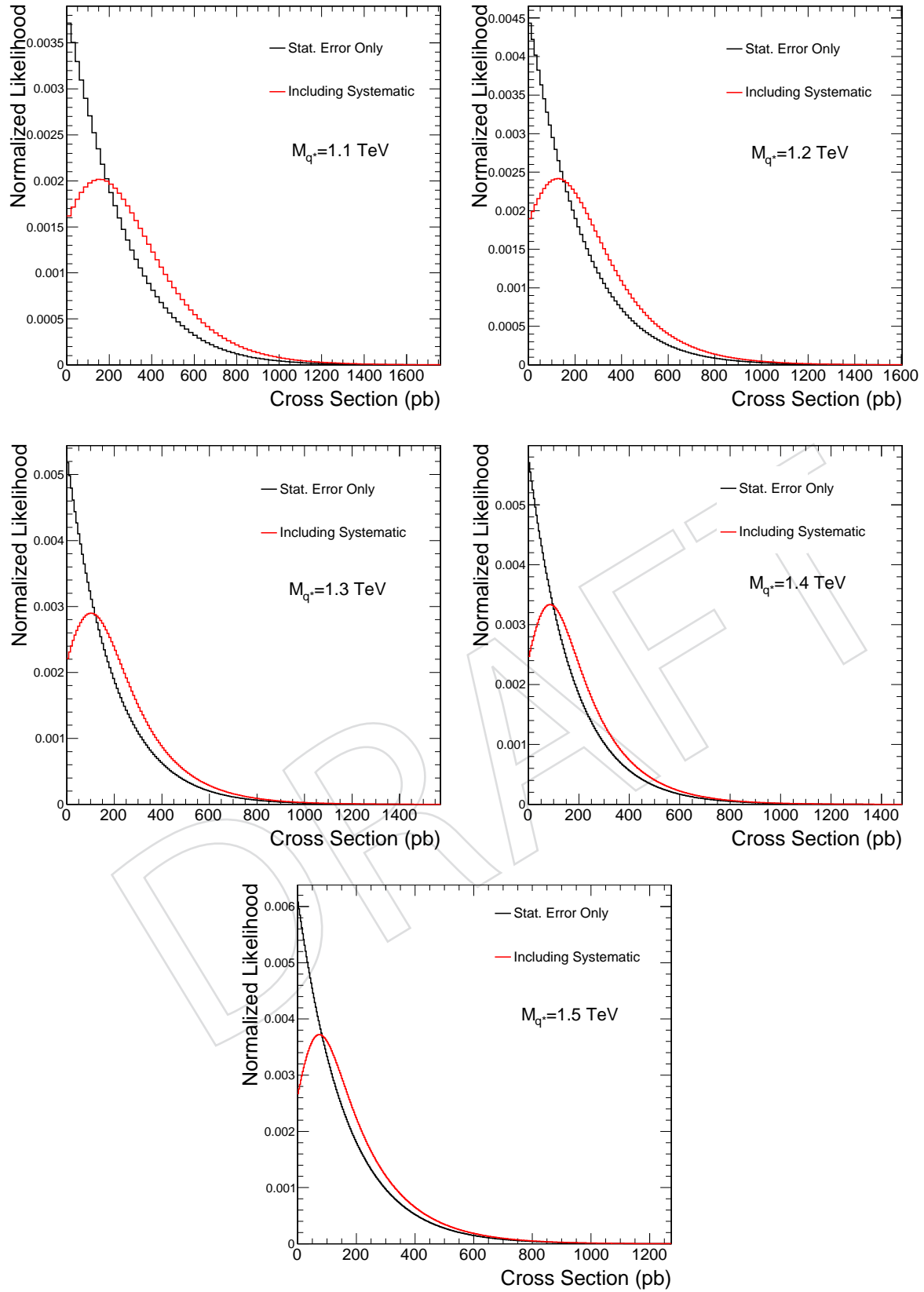


Figure 36: Likelihood distribution with %95 C.L. cross section limit at various excited quark resonance masses including systematics. Black line is %95 C.L. cross section limit with statistical error only. Red line shows %95 C.L. cross section limit with including systematics.

References

- [1] S. Ozturk, C. Jeong, S. Lee et al., “Plans to Search for New Particles Decaying to Dijets in pp Collisions at $\sqrt{s}=10$ TeV”, *CMS AN- 2009/070 HYPERLINK* (2009).
- [2] C. Jeong, S. Lee, I. Volobuev et al., “Dijet Resonance Shapes for $\sqrt{s}=10$ TeV”, *CMS AN- 2009/145 HYPERLINK* (2009).
- [3] K. Gumus, N. Akcshurin, S. Esen et al., “CMS Senitivity to Dijet Resonances”, *CMS Note 2006/070 HYPERLINK* (2006).
- [4] A. Harel, J. Hirschauer, S. E. Koylu et al., “Search for New Physics with the Dijet Centrality Ratio”, *CMS AN- 2010/126 HYPERLINK* (2010).
- [5] A. Bhatti et al., “CMS search plans and sensitivity to new physics with dijets”, *J. Phys. G* **36** (2009) 015004, [arXiv:0807.4961](#). doi:10.1088/0954-3899/36/1/015004.
- [6] U. Baur, I. Hinchliffe, and D. Zeppenfeld, “EXCITED QUARK PRODUCTION AT HADRON COLLIDERS”, *Int. J. Mod. Phys. A* **2** (1987) 1285.
- [7] J. Bagger, C. Schmidt, and S. King, “AXIGLUON PRODUCTION IN HADRONIC COLLISIONS”, *Phys. Rev. D* **37** (1988) 1188.
- [8] R. S. Chivukula, A. G. Cohen, and E. H. Simmons, “New Strong Interactons at the Tevatron?”, *Phys. Lett. B* **380** (1996) 92–98, [arXiv:hep-ph/9603311](#).
- [9] J. L. Hewett and T. G. Rizzo, “LOW-ENERGY PHENOMENOLOGY OF SUPERSTRING INSPIRED E(6) MODELS”, *Phys. Rept.* **183** (1989) 193.
- [10] L. Randall and R. Sundrum, “Large Mass Hierarchy from a Small Extra Dimension”, *Phys. Rev. Lett.* **83** (1999) 3370.
- [11] E. Eichten, I. Hinchliffe, K. D. Lane et al., “SUPER COLLIDER PHYSICS”, *Rev. Mod. Phys.* **56** (1984) 579–707.
- [12] CDF Collaboration, T. Aaltonen et al., “Search for new particles decaying into dijets in proton- antiproton collisions at $\sqrt{s} = 1.96$ TeV”, *Phys. Rev. D* **79** (2009) 112002, [arXiv:0812.4036](#). doi:10.1103/PhysRevD.79.112002.
- [13] D0 Collaboration, V. M. Abazov et al., “Search for new particles in the two-jet decay channel with the D0 detector”, *Phys. Rev. D* **69** (2004) 111101, [arXiv:hep-ex/0308033](#).
- [14] CDF Collaboration, F. Abe et al., “Search for new particles decaying to dijets at CDF”, *Phys. Rev. D* **55** (1997) 5263–5268, [arXiv:hep-ex/9702004](#).